

000 001 002 003 004 005 006 007 008 009 010 011 012 013 014 015 016 017 018 019 020 021 022 023 024 025 026 027 028 029 030 031 032 033 034 035 036 037 038 039 040 041 042 043 044 045 046 047 048 049 050 051 052 053 LIVE~~MOMENTS~~: RESELECTED KEY PHOTO RESTORATION IN LIVE PHOTOS VIA REFERENCE-GUIDED DIFFUSION

Anonymous authors

Paper under double-blind review

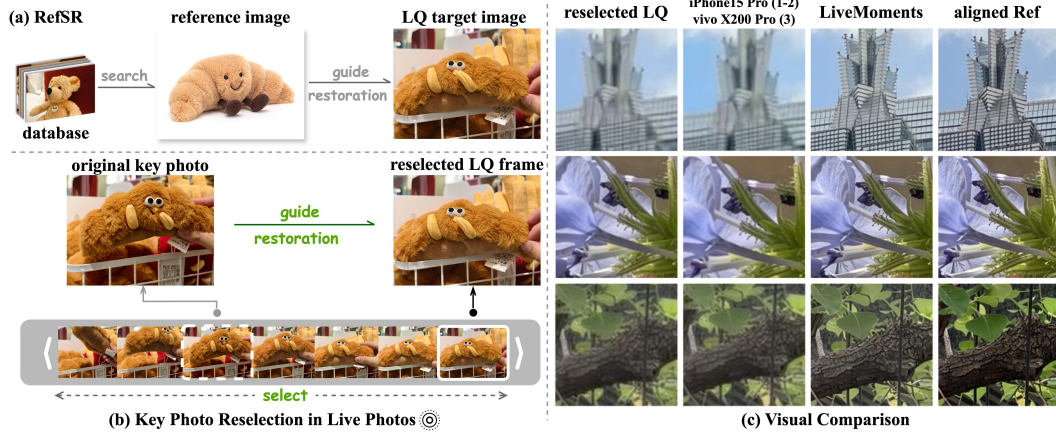


Figure 1: Illustration of Reselected Key Photo Restoration in Live Photos and visual comparison. While RefISR adopts external reference image with only semantic similarity, our setting leverages both the reference and target images from the same Live Photo sequence, ensuring a shared temporal context. The proposed **LiveMoments** significantly outperforms the premium smartphones.

ABSTRACT

Live Photo captures both a high-quality key photo and a short video clip to preserve the precious dynamics around the captured moment. While users may choose alternative frames as the key photo to capture better expressions or timing, these frames often exhibit noticeable quality degradation, as the photo capture ISP pipeline delivers significantly higher image quality than the video pipeline. This quality gap highlights the need for dedicated restoration techniques to enhance the reselected key photo. To this end, we propose *LiveMoments*, a reference-guided image restoration framework tailored for the reselected key photo in Live Photos. Our method employs a two-branch neural network: a reference branch that extracts structural and textural information from the original high-quality key photo, and a main branch that restores the reselected frame using the guidance provided by the reference branch. Furthermore, we introduce a unified Motion Alignment module that incorporates motion guidance for spatial alignment at both the latent and image levels. Experiments on real and synthetic Live Photos demonstrate that *LiveMoments* significantly improves perceptual quality and fidelity over existing solutions, especially in scenes with fast motion or complex structures.

1 INTRODUCTION

Unlike traditional photographs that capture a static frame, a Live Photo preserves the fleeting moments around a shutter click. To achieve this, each Live Photo consists of two components: (a) a high-quality (HQ) key photo¹ taken at the capture moment and (b) a low-quality (LQ) video clip approximately

¹From Apple's official documentation: <https://support.apple.com/en-sg/104966>

054 3 seconds, spanning moments around the key photo. This format not only enables dynamic visual
 055 recording, but also offers the flexibility for users to reselect a preferred frame as the new key photo.
 056 However, these reselected frames often exhibit significantly reduced quality. While the original key
 057 photo is processed through the complete ISP pipeline with advanced enhancements, the alternative
 058 frames are extracted from a compressed, low-latency preview stream and are further degraded by
 059 motion blur and sensor noise. To ensure optimal user experience, it is essential to restore the quality
 060 of the reselected frame to match that of the original key photo, while preserving content fidelity.

061 To this end, we introduce a new task: **Reselected Key Photo Restoration in Live Photos**, where the
 062 original key photo serves as a reference to guide the restoration of the reselected frame. We position
 063 this task as a sub-category of Reference-based Super-Resolution (RefSR), with a unique setting that
 064 restores a single LQ frame guided by a single reference from the same Live Photo sequence. Unlike
 065 conventional Reference-based Image Super-Resolution (RefISR), which restores the LQ image with
 066 an HQ reference from external databases, our task leverages an in-sequence reference that ensures
 067 content consistency. Meanwhile, Reference-based Video SR (RefVSR) enhances full video sequences
 068 but struggles with high-resolution inputs (*i.e.*, 4K), and methods are typically built on triple-camera
 069 smartphone datasets, with videos from different fields of view recorded simultaneously. In contrast,
 070 our task focuses on real Live Photos, where a single 4K frame is restored with guidance from a
 071 temporally offset reference. This setting naturally involves more dynamic real-world scenes, making
 072 it novel and practical while remaining efficient in both time and memory. Furthermore, our task
 073 introduces unique challenges, including significant quality gap and motion misalignment between the
 074 reselected frame and the original key photo, due to subject movement or camera shake.

075 These challenges impose limitations on existing RefSR methods for the task of reselected key photo
 076 restoration. Traditional RefISR methods, typically based on CNNs or transformers (Zhang et al.,
 077 2019; Jiang et al., 2021), adopt various feature matching strategies but are constrained by relatively
 078 small model size and the lack of strong pre-trained priors, making them insufficient for handling the
 079 diverse degradations and motion misalignments in Live Photos. Although diffusion-based RefISR
 080 methods demonstrate stronger generative capabilities, only two such methods have been explored
 081 to date and often produce unnatural textures. ReFIR (Guo et al., 2024) relies on a fixed-coefficient
 082 gating mechanism with limited robustness, while CoSeR (Sun et al., 2024) generates HQ references
 083 from CLIP-based embeddings that neglect local detail alignment and fuses features by prioritizing
 084 LR content, making it less suitable for reference-driven tasks. Beyond image-based settings, RefVSR
 085 methods remain confined to traditional designs and exploit full sequence (Lee et al., 2022) or single
 086 middle-frame (Kim et al., 2023) references with temporal propagation. Such designs are utilized to
 087 handle small misalignments but fail under the larger temporal offsets and quality gaps in Live Photos.
 088 In addition, single image SR (SISR) methods (Wang et al., 2024; Wu et al., 2024b) overlook the
 089 reference and often fail to preserve accurate structure and details in the presence of motion.

090 Therefore, we propose LiveMoments, a diffusion-based framework tailored for reselected key photo
 091 restoration in Live Photos. It leverages diffusion priors for fine-grained feature extraction and employs
 092 attention-based fusion to guide the RestorationNet in selectively incorporating well-aligned reference
 093 features within a shared feature space, enabling precise and targeted reference-driven conditioning.
 094 To address motion misalignment between the two inputs, we further introduce a unified Motion
 095 Alignment module that operates at both the latent and image levels. At the latent level, we propose a
 096 *motion-guided attention* that injects spatially aligned guidance into the latent space for more coherent
 097 feature fusion. At the image level, we design a *patch correspondence retrieval* strategy that captures
 098 patch-wise motion to locate the corresponding reference patches for consistent restoration in ultra-
 099 high-resolution frames. To facilitate fair evaluation, we introduce a comprehensive benchmark for this
 100 task, including a synthetic dataset, SynLive260, and two real-world Live Photo datasets, vivoLive144
 101 and iPhoneLive90, captured by consumer smartphones across diverse scenes. Furthermore, we adapt
 102 the no-reference metrics originally used in SISR and image generation to better suit our setting, where
 103 a HQ reference is available for evaluating result quality.

104 Our contributions can be summarized as follows:
 105

- 106 • To the best of our knowledge, we are the first to address the problem of reselected key photo
 107 restoration in Live Photos. We propose LiveMoments, a diffusion-based framework tailored for this
 108 task, which leverages a dual-branch neural network with advanced feature fusion.
- 109 • To mitigate spatial misalignment in Live Photos, a unified Motion Alignment module is introduced
 110 to inject the motion guidance at the latent level while ensuring image-level content consistency.

108 • We establish a comprehensive benchmark consisting of three datasets and task-specific metrics.
 109 Extensive experiments show that LiveMoments significantly outperforms state-of-the-art RefSR and
 110 SISR methods in both quantitative and visual results, even under challenging real-world scenarios.
 111

112 **2 RELATED WORK**
 113

114 **2.1 DIFFUSION-BASED SINGLE IMAGE SUPER-RESOLUTION (SISR)**
 115

116 Diffusion-based SISR restores the HQ images from a single LQ input via diffusion models, with
 117 recent research focusing on complex and unknown degradations. Building on the remarkable
 118 generative capabilities of diffusion models demonstrated in text-to-image (T2I) tasks (Rombach
 119 et al., 2022; Podell et al., 2023), recent works (Wang et al., 2024; Lin et al., 2024; Wu et al., 2024b;
 120 Yu et al., 2024) adapt these pretrained backbones to SISR by leveraging control mechanisms (e.g.,
 121 ControlNet (Zhang et al., 2023b)). StableSR (Wang et al., 2024) fine-tunes a time-aware encoder with
 122 the controllable feature warping module, while SeeSR (Wu et al., 2024b) uses degradation-aware
 123 text prompts. SUPiR (Yu et al., 2024) scales up generation by integrating large diffusion backbones
 124 with high-capacity adapters and datasets. CoSeR (Sun et al., 2024) utilizes a pre-trained T2I model
 125 to generate HQ references from LR embeddings for guided restoration. More recently, one-step
 126 distillation techniques are adopted to significantly reduce the number of diffusion steps by directly
 127 initializing from the LQ input. OSEDiff (Wu et al., 2024a) utilizes VSD loss (Wang et al., 2023b) as
 128 a regularization term, while TSD-SR (Dong et al., 2024) distills a multi-step SD3 model (Esser et al.,
 129 2024) into a one-step SISR solution via target score distillation. Despite these advances, most of the
 130 existing methods rely solely on generative priors and may produce visually plausible yet inaccurate
 131 content that sacrifice fidelity for perceptual richness. Such methods often fail to produce accurate
 132 results in real-world scenarios, where effectively preserving the original visual content is essential.
 133

134 **2.2 REFERENCE-BASED SUPER-RESOLUTION (REFSR)**
 135

136 RefSR aims to enhance LR inputs by leveraging external HR references. Image-based RefSR (RefISR)
 137 addresses single-image restoration and primarily focus on establishing accurate correspondence
 138 between the LR input and the reference image, enabling effective texture transfer and detail refinement.
 139 Early methods explore various matching strategies, including feature warping (Zheng et al., 2018),
 140 patch-level matching (Zhang et al., 2019; Yang et al., 2020), and multi-reference fusion (Zhang
 141 et al., 2023a). In addition, SSEN (Shim et al., 2020) employs deformable convolution (Dai et al.,
 142 2017) for adaptive feature alignment. Building on this, C2-Matching (Jiang et al., 2021) introduces a
 143 contrastive correspondence network with teacher-student correlation distillation, while DATSR (Cao
 144 et al., 2022) integrates deformable convolution with the Swin Transformer for enhanced performance.
 145 Recently, ReFIR (Guo et al., 2024) proposes a retrieval-enhanced architecture built on diffusion-based
 146 SISR models, achieving reference-guided texture propagation without additional training. Video-
 147 based RefSR (RefVSR) extends reference-based techniques to video super-resolution on smartphone
 148 datasets, where triple-camera systems simultaneously record videos from different fields of view.
 149 By leveraging consecutive frames, these methods integrate multi-frame information with reference
 150 to enhance restoration, with only minimal time gaps between frames and the reference. Methods
 151 such as RefVSR (Lee et al., 2022) and RefVSR++(Zou et al., 2025) employ the entire HQ video
 152 sequence as reference and exploit bidirectional propagation to align multi-frame information, while
 153 ERVSR (Kim et al., 2023) improves efficiency by leveraging only a single reference frame. While
 154 our setting can be regarded as a sub-category of RefSR, it departs from conventional paradigms in
 155 both dataset construction and task formulation. To address the unique challenges posed in Live Photo,
 156 we construct dedicated datasets and design task-specific architectures.
 157

158 **3 METHOD**
 159

160 **3.1 PRELIMINARY**
 161

162 Given a Live Photo, we denote the reselected LQ frame as $I_{Ls} \in \mathbb{R}^{H \times W \times 3}$ and the original HQ
 163 key photo as $I_{Ho} \in \mathbb{R}^{H \times W \times 3}$. The goal of our task is to reconstruct a high-quality version of the
 164 reselected frame, denoted as \tilde{I}_{Hs} , that matches the visual quality of I_{Ho} while preserving the content

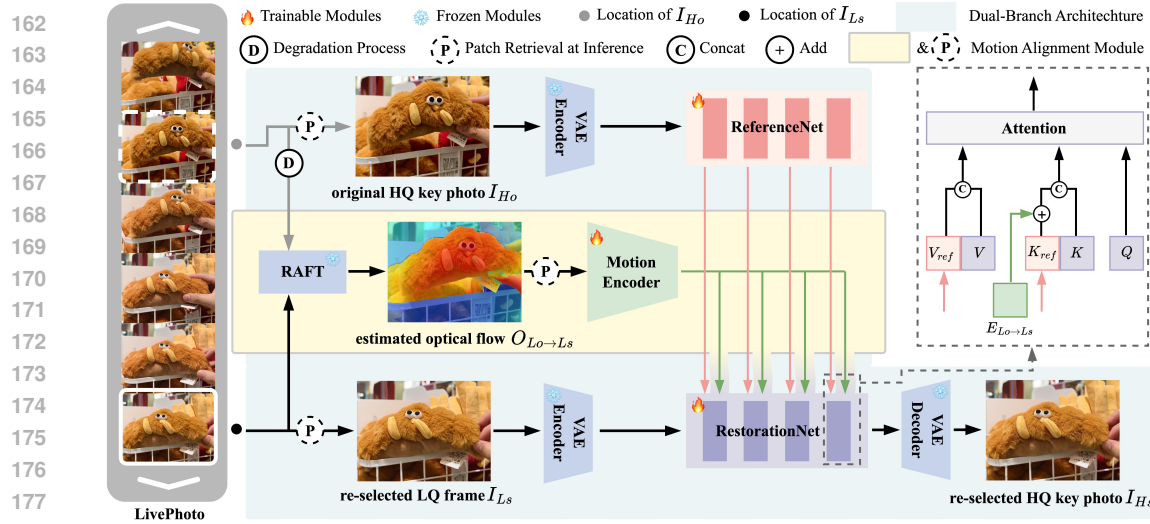


Figure 2: Overall architecture of LiveMoments. After the fixed VAE encoder, the original key photo and the re-selected LQ frame are fed into the ReferenceNet and RestorationNet, respectively, and fused via cross-attention. For latent level motion alignment, the optical flow is estimated with a fixed RAFT model and encoded with a Motion Encoder, which is further injected into the cross-attention as an additive bias. For image level alignment, Patch Correspondence Retrieval (PCR) strategy is adopted during the inference to ensure spatial consistency when using the tiling strategy.

fidelity of I_{Ls} . Thus, the task is formulated as learning a restoration model G_θ parameterized by θ , which takes (I_{Ls}, I_{Ho}) as input and predicts \tilde{I}_{Hs} .

Since real-world Live Photos lack HQ ground-truth counterparts for reselected frames, we construct the training dataset using HQ video sequences. For example, the ground-truth I_{Hs} of the reselected frame and the original key photo I_{Ho} are extracted with a clear temporal gap. I_{Hs} is degraded to produce the LQ reselected frame I_{Ls} (see Section 4.1 for more details). We employ flow matching (Albergo & Vanden-Eijnden, 2022; Esser et al., 2024) to train the diffusion model. Flow matching aims to transform Gaussian noise into a target distribution by learning an appropriate velocity field. In particular, Rectified Flow defines the forward process as $x_t = \alpha(t)x_0 + \beta(t)\epsilon$, where $\alpha(t) = 1 - t$ and $\beta(t) = t$. The training objective is $\mathbb{E}_{t, x_t} \|f(x_t) - dx_t/dt\|_2^2$, where f denotes the neural network that parameterizes the velocity field in the Rectified Flow. To adapt flow matching to image-to-image translation tasks, several approaches condition the generation process on a source image, aiming to synthesize the target image from Gaussian noise. However, these methods often suffer from issues such as hallucinated textures. Inspired by bridge matching (Chadebec et al., 2025; Liu et al., 2023; Shi et al., 2023) that directly learns the velocity field between the source and target distributions, we leverage an objective that focuses on learning the velocity field between I_{Ls} and I_{Hs} . Specifically, we define the forward process as:

$$z_t = \alpha(t)z_{Hs} + \beta(t)z_{Ls} + \sigma(t)\epsilon, \quad (1)$$

where z_{Hs} and z_{Ls} are the latent representations obtained by a VAE encoder in the setting of latent diffusion. The objective is to learn the velocity field:

$$\mathcal{L}_\theta = \mathbb{E}_{t, z_t} \|G_\theta(z_t, t) - \frac{dz_t}{dt}\|_2^2. \quad (2)$$

The details of $\alpha(t), \beta(t), \sigma(t)$ can be found in the *supplementary material*.

3.2 OVERVIEW OF LIVEMOMENTS

Our setting is characterized by temporal dependency and reference-target correlation. Specifically, the reference and degraded frames are sampled from the same Live Photo sequence with a clear temporal offset, yet they retain scene-level coherence compared to static or externally sourced references. Consequently, effective restoration of the reselected key photo requires leveraging fine-grained details from the reference frame. To achieve this, the proposed LiveMoments consists of three key components, as shown in Fig. 2: a RestorationNet performs conditional denoising on the noisy latent

216 of I_{Ls} ; a ReferenceNet encodes the original key photo I_{Ho} to provide high-quality guidance; a unified
 217 Motion Alignment module achieves fine-grained alignment at both the latent and image levels.
 218

219 **3.3 DUAL-BRANCH ARCHITECTURE**
 220

221 Inspired by the success of reference-guided generation in video tasks (Hu, 2024; Xu et al., 2024),
 222 we adopt a similar dual-branch design for reference-based restoration, leveraging both the diffusion
 223 priors and the attention mechanisms of the pre-trained T2I diffusion models. Unlike CLIP-based
 224 structure (Radford et al., 2021), which focuses on global semantics for low-resolution inputs, the
 225 ReferenceNet preserves high-resolution features and fine-grained details that are essential for high-
 226 fidelity restoration. Structurally, it mirrors the denoising backbone, enabling weight initialization from
 227 pre-trained checkpoints and better feature alignment with the RestorationNet. In our implementation,
 228 both branches are built on the Stable Diffusion 3 (SD3) architecture (Esser et al., 2024), which
 229 provides a powerful generation backbone. The original key photo I_{Ho} is first encoded into the latent
 230 space by a frozen VAE encoder, then processed by a DiT-based ReferenceNet to obtain detailed
 231 features. These features are integrated into the main branch through cross-attention, where the key
 232 and value from both branches are concatenated as follows:
 233

$$\text{Cross_attn} = \text{Softmax} \left(\frac{Q[K, K_{\text{ref}}]^\top}{\sqrt{d}} \right) [V, V_{\text{ref}}], \quad (3)$$

234 where Q is the query from the attention layer of the RestorationNet, K_{ref} and V_{ref} are the key and
 235 value from the ReferenceNet, while K and V are those from the RestorationNet. $[\cdot, \cdot]$ denotes the
 236 concatenation operation, and d is the channel dimension. This interaction enables the model to
 237 adaptively select and transfer textures and structural information from the reference image rather than
 238 relying solely on coarse semantic alignment.
 239

240 **3.4 MOTION ALIGNMENT MODULE**
 241

242 **3.4.1 LATENT SPACE MOTION ALIGNMENT**
 243

244 While the dual-branch structure enables implicit feature matching and detailed information transfer,
 245 it is often insufficient for the task of reselected key photo restoration on Live Photos. The reselected
 246 frame I_{Ls} typically suffers from motion blur and subject displacement, making it difficult to establish
 247 accurate correspondences and align with the original key photo. Moreover, the significant quality
 248 gap between the HQ key photo and the degraded reselected frame further hinders effective feature
 249 alignment and leads to unreliable fusion.
 250

251 To address these challenges, we design a *motion-guided attention* that introduces explicit motion
 252 guidance into the latent space. In Live Photos, where temporal dependency naturally exists, optical
 253 flow serves as an intuitive mechanism for establishing spatial correspondence. Distinct from previous
 254 flow-based restoration methods, we transform the estimated flow into motion embeddings and
 255 incorporate them into the cross-attention, thereby providing alignment priors to guide attention
 256 toward relevant regions. Specifically, we utilize a pre-trained RAFT model (Teed & Deng, 2020)
 257 to estimate the optical flow $O_{Lo \rightarrow Ls}$, which serves as a dense pixel displacement field between the
 258 degraded original key photo I_{Lo} and the reselected LQ frame I_{Ls} . During training, I_{Lo} is synthesized
 259 by applying the same degradation parameters as those used for the reselected frame I_{Ls} . At inference
 260 time, since I_{Ls} suffers from real-world degradation in Live Photos, we simulate the corresponding
 261 degradation on I_{Ho} to narrow the quality gap and obtain more reliable motion estimation. To encode
 262 the estimated motion, we introduce a lightweight Motion Encoder with convolutional layers and
 263 SiLU activations that transforms the raw flow field into motion embeddings. These embeddings are
 264 then incorporated into the cross-attention mechanism as an additive bias to the reference key features:
 265

$$\text{Cross_attn}_{\text{opt}} = \text{Softmax} \left(\frac{Q[K, K_{\text{ref}} + E_{Lo \rightarrow Ls}]^\top}{\sqrt{d}} \right) [V, V_{\text{ref}}], \quad (4)$$

266 where $E_{Lo \rightarrow Ls}$ denotes the motion embeddings derived from the dense pixel displacement field
 267 $O_{Lo \rightarrow Ls}$. The encoded relative motion acts as a spatial bias that facilitates the query to attend to
 268 aligned regions, thereby improving restoration under misaligned scenarios.
 269

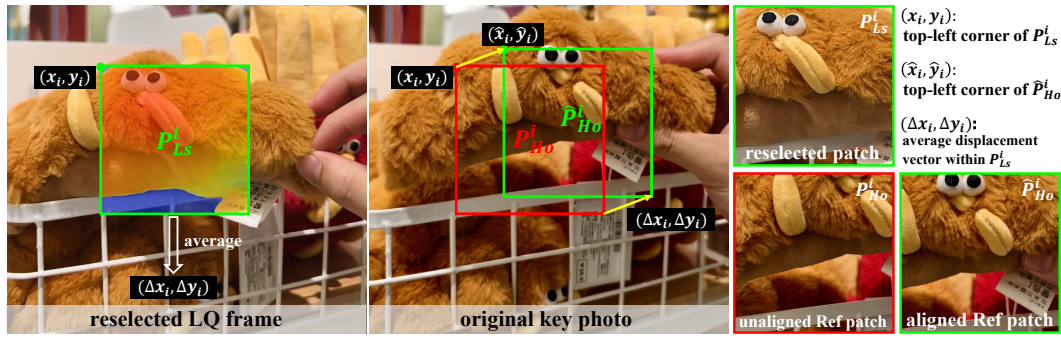


Figure 3: Illustration of the proposed Patch Correspondence Retrieval (PCR) strategy. The average displacement within a patch (the dense displacement field contained in P_{Ls}^i) is used to shift the top-left corner (x_i, y_i) to (\hat{x}_i, \hat{y}_i) , then we crop the aligned reference patch \hat{P}_{Ho}^i from I_{Ho} . On the right, we compare the reselected patch P_{Ls}^i , unaligned Ref patch P_{Ho}^i and the aligned Ref patch \hat{P}_{Ho}^i .

3.4.2 IMAGE SPACE MOTION ALIGNMENT

Live Photos typically have ultra-high resolutions (*i.e.*, 3072×4096 for the original key photo), which require patch-wise inference through a tiling strategy due to GPU memory limits. However, subject motion often causes pixel-level misalignment between patches of I_{Ls} and I_{Ho} , leading to content inconsistency that undermines reference-guided restoration. To mitigate this issue, and as a complement to motion-guided attention, we propose a *Patch Correspondence Retrieval (PCR)* strategy to stabilize local matching and improve content alignment between the reselected patches from I_{Ls} and the reference patches from I_{Ho} during inference. **Integrated into the tiling process and applied before the VAE encoder, it uses the estimated displacement field to locate the reference patch, ensuring that latent-space processing operates on spatially aligned inputs.** Unlike pixel-wise warping, the proposed alignment is performed at the patch level rather than on individual pixels, which is consistent with the tiling-based inference pipeline and naturally preserves spatial consistency. As shown in Fig. 3, we first estimate the optical flow $O_{Ls \rightarrow Ho}$ from I_{Ls} to I_{Ho} . For a patch $P_{Ls}^i \in \mathbb{R}^{p \times p \times 3}$ cropped from I_{Ls} with the standard tiling strategy, we compute the average displacement vector within the patch as:

$$(\Delta x_i, \Delta y_i) = \left(\frac{1}{p^2} \sum_{j=1}^{p \times p} f_{x_i}^j, \frac{1}{p^2} \sum_{j=1}^{p \times p} f_{y_i}^j \right), \quad (5)$$

where $(f_{x_i}^j, f_{y_i}^j)$ represents the x- and y-axis components of the dense displacement field at pixel j , obtained from $O_{Ls \rightarrow Ho}$. The top-left corner (\hat{x}_i, \hat{y}_i) of the aligned reference patch \hat{P}_{Ho}^i , cropped from I_{Ho} , is then computed by shifting the top-left corner (x_i, y_i) of P_{Ls}^i :

$$(\hat{x}_i, \hat{y}_i) = (x_i + \Delta x_i, y_i + \Delta y_i). \quad (6)$$

The aligned reference patch \hat{P}_{Ho}^i is then cropped from I_{Ho} with the patch size p . As shown in Fig. 3, \hat{P}_{Ho}^i achieves content consistency with P_{Ls}^i , compared to the unaligned reference patch that directly cropped from the same spatial location as P_{Ls}^i . With the tiling strategy, the corresponding optical flow patch is cropped at the same location as \hat{P}_{Ho}^i to ensure spatial consistency of the network inputs.

4 EXPERIMENT

4.1 EXPERIMENTAL SETTINGS

Training Datasets. Since there are no existing datasets specifically for reselected key photo restoration in Live Photos, we construct the training set based on high-quality video data. For each sample, we select the HQ ground truth I_{Hs} of the reselected frame and the original key photo I_{Ho} with a clear temporal gap. In particular, we extract frames from the first 3,000 videos of the 2K-resolution DL3DV dataset (Ling et al., 2024), a large and multi-view video dataset covering over 10,000 scenes. The frame interval is set to 5, resulting in 50,400 image pairs at a resolution of 1024×1024 . To further

324 Table 1: Quantitative comparison with RefSR and SISR methods on real-world Live Photo datasets.
325 The best results are highlighted in **bold**. Here, NI_{re} denotes $NIQE_{re}$, MU_{re} denotes $MUSIQ_{re}$, CA_{re}
326 denotes CLIPQA and MA_{re} denotes MANIQA.
327

Method	vivoLive144					iPhoneLive90						
	$NI_{re} \downarrow$	$MU_{re} \downarrow$	$CA_{re} \downarrow$	$MA_{re} \downarrow$	CLIP-Q↑	DINO-Q↑	$NI_{re} \downarrow$	$MU_{re} \downarrow$	$CA_{re} \downarrow$	$MA_{re} \downarrow$	CLIP-Q↑	DINO-Q↑
TTSR	0.2050	0.3545	0.1928	0.1400	0.9626	0.8304	0.3069	0.2858	0.2593	0.1974	0.9505	0.8689
C2-Matching	0.2047	0.3512	0.1929	0.1390	0.9623	0.8298	0.3147	0.2800	0.2791	0.1978	0.9505	0.8685
DATSR	0.2212	0.3573	0.1951	0.1386	0.9621	0.8261	0.3324	0.2859	0.2853	0.1963	0.9500	0.8657
MRefSR	0.2276	0.3537	0.1916	0.1371	0.9616	0.8216	0.3408	0.2845	0.2900	0.1978	0.9499	0.8652
CoSeR	0.1953	0.1865	0.2752	0.1080	0.9658	0.9197	0.1774	0.2492	0.1564	0.0784	0.9608	0.8618
ReFIR (SeeSR)	0.3258	0.3042	0.8606	0.2731	0.9582	0.8156	0.2895	0.3605	0.5111	0.1429	0.9467	0.7319
ReFIR (SUPIR)	0.4665	0.2318	0.3571	0.1559	0.9201	0.8783	0.4336	0.2778	0.2224	0.0876	0.9190	0.8105
RefVSR	0.3798	0.3157	0.2142	0.1967	0.9609	0.8385	0.4226	0.2326	0.3016	0.2810	0.9472	0.8431
ERVSR	0.3314	0.4012	0.3457	0.1459	0.9597	0.8137	0.3635	0.3188	0.4569	0.2030	0.9448	0.8607
StableSR	0.3032	0.2833	0.7447	0.2250	0.9458	0.8491	0.2571	0.3566	0.3837	0.1253	0.9466	0.8174
DiffBIR	0.4228	0.3213	0.9547	0.3550	0.9023	0.7769	0.3477	0.3532	0.5397	0.1705	0.9145	0.7727
SeeSR	0.2767	0.2916	0.8168	0.2331	0.9606	0.8269	0.2957	0.3511	0.5174	0.1408	0.9445	0.7253
SUPIR	0.2703	0.2545	0.8275	0.1115	0.9407	0.8559	0.1805	0.3429	0.4924	0.0738	0.9422	0.7908
OSEDiff	0.2694	0.3191	0.8206	0.2444	0.9541	0.8536	0.2750	0.3832	0.4698	0.1260	0.9444	0.7525
TSD-SR	0.3359	0.3133	0.8519	0.2205	0.9476	0.8636	0.2963	0.3956	0.5142	0.1210	0.9477	0.7917
LiveMoments	0.0990	0.0893	0.0809	0.0556	0.9805	0.9629	0.0801	0.1230	0.1361	0.0543	0.9842	0.9466

341 enrich the dataset with various motion patterns, we additionally collect 4K videos from the internet,
342 obtaining 25,000 image pairs at the same resolution. To simulate degradations in Live Photo videos,
343 we utilize the Real-ESRGAN (Wang et al., 2021) pipeline to obtain the LQ reselected frame I_{Ls} , with
344 parameters specifically adjusted to better align the real-world degradations in mobile photography.

345 **Test Datasets.** For model evaluation, we construct a synthesized dataset, **SynLive260**, along with two
346 real-world Live Photo datasets, **vivoLive144** and **iPhoneLive90**, collected from high-end consumer
347 smartphones. VivoLive144 and iPhoneLive90 consist of 144 and 90 Live Photos captured with vivo
348 X200 Pro and iPhone 15 Pro, respectively. In both datasets, the LQ reselected frames are manually
349 extracted from the associated Live Photo video clips. **These two datasets cover diverse dynamic**
350 **scenes, including indoor and outdoor environments, street views, portraits, pets, and everyday objects,**
351 **with motions from camera movement and subject dynamics.** SynLive260 is built from 182 internet
352 videos, covering various scenarios. After frame extraction, we obtain 260 image pairs of the HQ
353 reselected frame and the original key photo. The HQ reselected frame is then degraded by Real-
354 ESRGAN pipeline with a $\times 2$ downsampling factor to simulate degradations in Live Photo videos.

355 **Evaluation Metrics.** On both the synthesized dataset and real-world Live Photo dataset, we adopt no-
356 reference metrics for evaluation. We apply four metrics originally designed for SISR: NIQE (Zhang
357 et al., 2015), MUSIQ (Ke et al., 2021), CLIPQA (Wang et al., 2023a), and MANIQA (Yang et al.,
358 2022). However, unlike traditional SR settings, our task provides access to the original high-quality
359 key photo I_{Ho} as a reference. This allows us to extend these metrics into a relative no-reference form
by computing the normalized deviation between the restored reselected frame \tilde{I}_{Hs} and I_{Ho} :

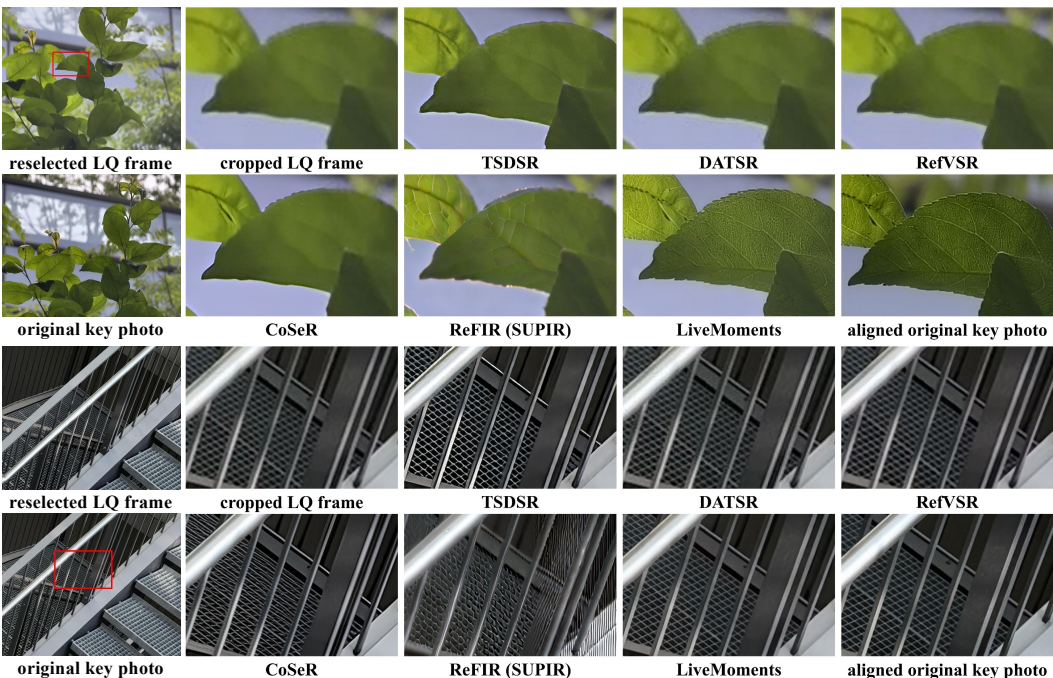
$$\text{metric}_{re}(\tilde{I}_{Hs}, I_{Ho}) = \frac{|\text{metric}(\tilde{I}_{Hs}) - \text{metric}(I_{Ho})|}{\text{metric}(I_{Ho})}, \quad (7)$$

360 where $\text{metric}(\cdot)$ denotes one of the above no-reference metrics. This formulation quantifies the
361 quality gaps between the restored image \tilde{I}_{Hs} and a known HQ reference. To further assess perceptual
362 alignment with I_{Ho} , we introduce two relative-reference metrics, CLIP-Q and DINO-Q, derived
363 from CLIP-I and DINO from DreamBooth (Ruiz et al., 2023). Following CLIPQA, we remove the
364 positional embeddings from both models to support high-resolution inputs and eliminate resizing-
365 induced distortions, which is crucial for faithful quality assessment. We also calculate full-reference
366 metrics on the synthesized dataset: PSNR, SSIM (Wang et al., 2004), LPIPS (Zhang et al., 2018)
367 and DISTs (Ding et al., 2020), where PSNR and SSIM are computed on y-channel in the YCbCr
368 space. FID is also evaluated on SynLive260. Since it requires downsampling 4K images to a low
369 resolution, we compute patch-wise FID by cropping images into 512×512 patches, which ensures
370 that the evaluation resolution is consistent with recent restoration works (Dong et al., 2024).

371 **Implementation Details.** Both the ReferenceNet and the RestorationNet are initialized from the
372 pre-trained weights of SD3-medium. We only train the MM-DiT backbones of both networks along
373 with the Motion Encoder, while keeping the VAE encoder and decoder frozen. Training starts with
374 an initial learning rate of $5e^{-5}$ and takes roughly 48h with 2 NVIDIA H20 GPUs and a batch size
375 of 8. **Inference is performed using a tiling strategy with a patch size of 1024×1024 , which is kept**
376 **identical to the training patch size for stable and fair evaluation.**

378 Table 2: Quantitative comparison with RefSR and SISR methods on the synthetic dataset SynLive260.
379 The best results are highlighted in **bold**. Here, NI_{re} denotes $NIQE_{re}$, MU_{re} denotes $MUSIQ_{re}$, CA_{re}
380 denotes CLIPQA and MA_{re} denotes MANIQA.
381

Method	PSNR↑	SSIM↑	LPIPS↓	DISTS↓	FID↓	NI_{re} ↓	MU_{re} ↓	CA_{re} ↓	MA_{re} ↓	CLIP-Q↑	DINO-Q↑
TTSR	31.74	0.8778	0.2416	0.1259	18.53	0.4254	0.3885	0.1996	0.2209	0.9621	0.8373
C2-Matching	31.85	0.8782	0.2419	0.1250	18.51	0.4354	0.3873	0.2051	0.2199	0.9619	0.8391
DATSR	31.84	0.8783	0.2417	0.1251	18.50	0.4380	0.3876	0.2034	0.2186	0.9618	0.8388
MRefSR	31.84	0.8782	0.2420	0.1252	18.73	0.4342	0.3886	0.2058	0.2195	0.9612	0.8374
CoSeR	27.60	0.8136	0.2436	0.1135	13.92	0.2603	0.2548	0.6380	0.1028	0.9699	0.8924
ReFIR (SeeSR)	27.44	0.7942	0.2873	0.1530	28.26	0.3378	0.4028	1.2814	0.1837	0.9558	0.7934
ReFIR (SUPIR)	24.20	0.7024	0.3992	0.1779	33.95	0.4968	0.3273	0.7808	0.1491	0.9238	0.8295
RefVSR	26.28	0.8037	0.2937	0.1183	15.10	0.3713	0.3003	0.1964	0.2783	0.9631	0.8609
ERVSR	26.26	0.8016	0.3335	0.1306	20.22	0.4035	0.4021	0.2819	0.2129	0.9576	0.8327
StableSR	26.49	0.7619	0.3238	0.1491	23.77	0.3912	0.3951	1.1322	0.1573	0.9464	0.8386
DiffBIR	25.98	0.6927	0.4421	0.1958	36.39	0.3771	0.4199	1.3705	0.2260	0.9167	0.7824
SeeSR	27.25	0.7865	0.2981	0.1571	28.89	0.3602	0.3929	1.2805	0.1853	0.9538	0.7940
SUPIR	25.96	0.7309	0.3660	0.1762	31.53	0.2875	0.3741	1.3061	0.1083	0.9335	0.7869
OSEDiff	26.81	0.7882	0.2915	0.1412	27.17	0.3325	0.4132	1.1931	0.1669	0.9566	0.8220
TSD-SR	25.34	0.7379	0.3090	0.1625	24.03	0.4081	0.4595	1.3084	0.1641	0.9439	0.8208
LiveMoments	31.65	0.8990	0.0828	0.0365	4.00	0.0911	0.0720	0.1155	0.0495	0.9950	0.9740



417 Figure 4: Visual comparison on the two real-world Live Photo datasets: vivoLive144 (top) and
418 iPhoneLive90 (bottom). The aligned original key photo is cropped manually for better comparison.
419

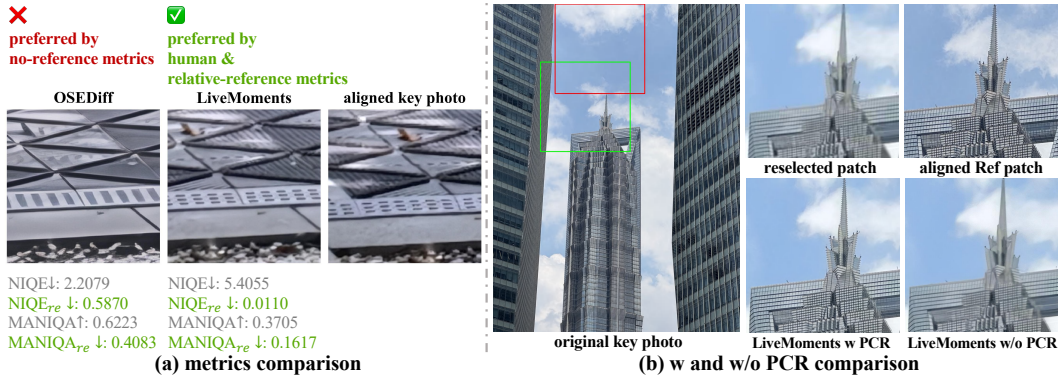
420 4.2 COMPARISON WITH EXISTING METHODS

421 We compare LiveMoments with three categories of state-of-the-art methods. First, RefISR methods
422 including TTSR (Yang et al., 2020), C2-Matching (Jiang et al., 2021), DATSR (Cao et al., 2022),
423 and MRefSR (Zhang et al., 2023a), as well as diffusion-based methods CoSeR (Sun et al., 2024) and
424 ReFIR (Yu et al., 2024) (based on SISR methods SeeSR and SUPIR). Designed for SISR, we replace
425 the synthesized reference in CoSeR with the actual one. Second, RefVSR methods RefVSR (Lee
426 et al., 2022) and ERVSR (Kim et al., 2023), for which we additionally supply full video inputs
427 to match their model design. Finally, recent diffusion-based SISR methods, including multi-step
428 (StableSR (Wang et al., 2024), DiffBIR (Lin et al., 2024), SeeSR (Wu et al., 2024b), SUPIR (Yu
429 et al., 2024)), and single-step (OSEDiff (Wu et al., 2024a), TSD-SR (Dong et al., 2024)).

430 **Real-World Live Photo Datasets.** The quantitative results on the two Live Photo datasets are shown
431 in Tab. 1, which can be found that our method achieves SOTA in both two datasets among all metrics.

432 Table 3: Ablation study of the network design on vivoLive144. All warp operation is applied on the
 433 original key photo, denoted as the reference image (Ref). The best results are highlighted in **bold**.

Method	NIQE _{re} ↓	CLIPQA _{re} ↓	MANIQA _{re} ↓	CLIP-Q↑	DINO-Q↑
RestorationNet	0.1677	0.2348	0.1105	0.9690	0.9081
RestorationNet + ReferenceNet	0.1097	0.0823	0.0631	0.9792	0.9539
RestorationNet + ReferenceNet + warp RefImage	0.1034	0.0873	0.0573	0.9774	0.9480
RestorationNet + ReferenceNet + warp RefLatent	0.1130	0.0850	0.0622	0.9776	0.9456
RestorationNet + ReferenceNet + warp RefKV	0.1183	0.0853	0.0657	0.9774	0.9437
LiveMoments (full model)	0.0990	0.0809	0.0556	0.9805	0.9629



452 Figure 5: (a) Comparison between no-reference metrics, the proposed relative no-reference metrics,
 453 and human visual preference in evaluating the proposed task. (b) Comparison between LiveMoments
 454 with (w) and without (w/o) the proposed Patch Correspondence Retrieval (PCR) strategy when
 455 processing 4K images. Patches are cropped for clearer visualization.

457 We note that commonly used no-reference metrics may be suboptimal for evaluating reference-guided
 458 restoration tasks, since they ignore the reference and often favor visually rich but inaccurate results.
 459 As illustrated in Fig. 5, a restored image with high quality scores but large deviation from the reference
 460 often contains visually implausible artifacts, whereas smaller deviations yield perceptually closer
 461 results. This reveals the limitation of no-reference metrics and highlights the effectiveness of the
 462 proposed relative no-reference metric. The visual results are provided in Fig. 4, where we compare
 463 representative methods with strong quantitative results. Our method effectively restores the reselected
 464 frame with details comparable to the original key photo without introducing artifacts, even when the
 465 input suffers from motion misalignment. More results are provided in the *supplementary material*.

466 **Synthetic Dataset.** The quantitative results on SynLive260 are shown in Tab. 2. It can be found that
 467 our method achieves the best performance among nearly all metrics. Although it shows lower PSNR,
 468 this mainly reflects the limitation of full-reference metrics in real-world restoration tasks, as discussed
 469 in (Yu et al., 2024). In contrast, the proposed task-specific metrics and qualitative comparisons (in
 470 the *supplementary material*) better capture the perceptual fidelity of the results.

4.3 ABLATION STUDY

474 **Effectiveness of the dual-branch architecture.** To validate the effectiveness of our dual-branch
 475 design, we first evaluate a baseline that uses only the RestorationNet without any reference guidance.
 476 As shown in the 1-st row of Tab. 3, performance drops across all metrics, highlighting the importance
 477 of introducing the ReferenceNet and the original key photo to enhance restoration quality.

478 **Effectiveness of the motion-guided attention.** We evaluate the effectiveness of our motion-guided
 479 attention by exploring different strategies for incorporating dense correspondence for motion align-
 480 ment into the network. Specifically, we evaluate a model without latent-level alignment and several
 481 variants that inject motion information at different stages of the ReferenceNet, as shown in rows
 482 2-5 in Tab. 3. All models are evaluated under our patch correspondence retrieval strategy to ensure
 483 spatial consistency during tiled inference on our vivoLive144 dataset. Among them, the proposed
 484 motion-guided attention outperforms other variants. This demonstrates the advantage of injecting
 485 alignment to guide the feature matching in the attention space, rather than relying on warping. We
 486 provide the results on SynLive260 in the *supplementary material*.

486 **Effectiveness of the Patch Correspondence Retrieval (PCR).** We present challenging case with
 487 large motion and complex textures that hinder patch-level alignment, to validate the effectiveness of
 488 PCR. As shown in Fig. 5, our method establishes accurate correspondence between the two inputs,
 489 leading to more consistent and visually coherent restoration. These results highlight the robustness of
 490 our strategy under real-world scenes. We provides more visual results in the *supplementary material*.
 491

492 5 CONCLUSION

493
 494 We propose LiveMoments, a diffusion-based network designed for reselected key photo restoration
 495 in Live Photos. LiveMoments employs a dual-branch neural network with cross-attention between
 496 the branches to transfer detailed structural and textural information from the original high-quality key
 497 photo to the reselected low-quality frame. To address the challenge of large motion misalignment,
 498 we introduce a unified Motion Alignment module that aligns motion between the reselected and
 499 original key photos in both the latent and image spaces. Furthermore, to facilitate comprehensive
 500 comparison, we present a comprehensive benchmark comprising both real and synthetic Live Photos,
 501 along with task-specific evaluation metrics. Extensive experiments on three datasets demonstrate that
 502 LiveMoments significantly outperforms existing methods across both quantitative metrics and visual
 503 quality, particularly in challenging scenarios.

504 505 ETHICS STATEMENT

506
 507 Our work focuses on restoring reselected key photos in Live Photos for improving mobile photography.
 508 The synthetic dataset SynLive260 is built from publicly available video sources with no personal
 509 information. The real-world datasets (vivoLive144 and iPhoneLive90) were collected with the
 510 consent of participants. Before public release, all identifiable faces will be removed or anonymized to
 511 minimize privacy concerns. Our method is not intended for identity recognition or generation, and
 512 the released resources will be restricted to academic research in image restoration. Potential misuse
 513 is minimal given the planned anonymization and the academic scope of this work.

514 515 REPRODUCIBILITY STATEMENT

516
 517 We provide implementation details in Sec. 4.1 and Appendix B, covering both training and inference.
 518 Details of dataset preparation and evaluation metrics are also included in Sec. 4.1. We plan to release
 519 our code and datasets to enable reproducibility and encourage further research.

521 REFERENCES

522 Michael S Albergo and Eric Vanden-Eijnden. Building normalizing flows with stochastic interpolants.
 523 *arXiv preprint arXiv:2209.15571*, 2022.

525 Jiezhang Cao, Jingyun Liang, Kai Zhang, Yawei Li, Yulun Zhang, Wenguan Wang, and Luc Van
 526 Gool. Reference-based image super-resolution with deformable attention transformer. In *European*
 527 *conference on computer vision*, pp. 325–342. Springer, 2022.

528 Clément Chadebec, Onur Tasar, Sanjeev Sreetharan, and Benjamin Aubin. Lbm: Latent bridge
 529 matching for fast image-to-image translation. *arXiv preprint arXiv:2503.07535*, 2025.

531 Jifeng Dai, Haozhi Qi, Yuwen Xiong, Yi Li, Guodong Zhang, Han Hu, and Yichen Wei. Deformable
 532 convolutional networks. In *Proceedings of the IEEE international conference on computer vision*,
 533 pp. 764–773, 2017.

534 Keyan Ding, Kede Ma, Shiqi Wang, and Eero P Simoncelli. Image quality assessment: Unifying
 535 structure and texture similarity. *IEEE transactions on pattern analysis and machine intelligence*,
 536 44(5):2567–2581, 2020.

538 Linwei Dong, Qingnan Fan, Yihong Guo, Zhonghao Wang, Qi Zhang, Jinwei Chen, Yawei Luo, and
 539 Changqing Zou. Tsd-sr: One-step diffusion with target score distillation for real-world image
 540 super-resolution. *arXiv preprint arXiv:2411.18263*, 2024.

540 Patrick Esser, Sumith Kulal, Andreas Blattmann, Rahim Entezari, Jonas Müller, Harry Saini, Yam
 541 Levi, Dominik Lorenz, Axel Sauer, Frederic Boesel, et al. Scaling rectified flow transformers for
 542 high-resolution image synthesis. In *Forty-first international conference on machine learning*, 2024.
 543

544 Hang Guo, Tao Dai, Zhihao Ouyang, Taolin Zhang, Yaohua Zha, Bin Chen, and Shu-tao Xia. Refir:
 545 Grounding large restoration models with retrieval augmentation. *Advances in Neural Information
 546 Processing Systems*, 37:46593–46621, 2024.

547 Li Hu. Animate anyone: Consistent and controllable image-to-video synthesis for character animation.
 548 In *Proceedings of the IEEE/CVF Conference on Computer Vision and Pattern Recognition*, pp.
 549 8153–8163, 2024.

550 Yuming Jiang, Kelvin CK Chan, Xintao Wang, Chen Change Loy, and Ziwei Liu. Robust reference-
 551 based super-resolution via c2-matching. In *Proceedings of the IEEE/CVF Conference on Computer
 552 Vision and Pattern Recognition*, pp. 2103–2112, 2021.

553 Junjie Ke, Qifei Wang, Yilin Wang, Peyman Milanfar, and Feng Yang. Musiq: Multi-scale image
 554 quality transformer. In *Proceedings of the IEEE/CVF international conference on computer vision*,
 555 pp. 5148–5157, 2021.

556 Youngrae Kim, Jinsu Lim, Hoonhee Cho, Minji Lee, Dongman Lee, Kuk-Jin Yoon, and Ho-Jin
 557 Choi. Efficient reference-based video super-resolution (ervsr): Single reference image is all you
 558 need. In *Proceedings of the IEEE/CVF Winter Conference on Applications of Computer Vision*, pp.
 559 1828–1837, 2023.

560 Junyong Lee, Myeonghee Lee, Sunghyun Cho, and Seungyong Lee. Reference-based video super-
 561 resolution using multi-camera video triplets. In *Proceedings of the IEEE/CVF conference on
 562 computer vision and pattern recognition*, pp. 17824–17833, 2022.

563 Xinqi Lin, Jingwen He, Ziyan Chen, Zhaoyang Lyu, Bo Dai, Fanghua Yu, Yu Qiao, Wanli Ouyang,
 564 and Chao Dong. Diffbir: Toward blind image restoration with generative diffusion prior. In
 565 *European Conference on Computer Vision*, pp. 430–448. Springer, 2024.

566 Lu Ling, Yichen Sheng, Zhi Tu, Wentian Zhao, Cheng Xin, Kun Wan, Lantao Yu, Qianyu Guo, Zixun
 567 Yu, Yawen Lu, et al. Dl3dv-10k: A large-scale scene dataset for deep learning-based 3d vision.
 568 In *Proceedings of the IEEE/CVF Conference on Computer Vision and Pattern Recognition*, pp.
 569 22160–22169, 2024.

570 Guan-Horng Liu, Arash Vahdat, De-An Huang, Evangelos A Theodorou, Weili Nie, and Anima
 571 Anandkumar. I²sb: Image-to-image schrödinger bridge. *arXiv preprint arXiv:2302.05872*,
 572 2023.

573 Dustin Podell, Zion English, Kyle Lacey, Andreas Blattmann, Tim Dockhorn, Jonas Müller, Joe
 574 Penna, and Robin Rombach. Sdxl: Improving latent diffusion models for high-resolution image
 575 synthesis. *arXiv preprint arXiv:2307.01952*, 2023.

576 Alec Radford, Jong Wook Kim, Chris Hallacy, Aditya Ramesh, Gabriel Goh, Sandhini Agarwal,
 577 Girish Sastry, Amanda Askell, Pamela Mishkin, Jack Clark, et al. Learning transferable visual
 578 models from natural language supervision. In *International conference on machine learning*, pp.
 579 8748–8763. PMLR, 2021.

580 Robin Rombach, Andreas Blattmann, Dominik Lorenz, Patrick Esser, and Björn Ommer. High-
 581 resolution image synthesis with latent diffusion models. In *Proceedings of the IEEE/CVF confer-
 582 ence on computer vision and pattern recognition*, pp. 10684–10695, 2022.

583 Nataniel Ruiz, Yuanzhen Li, Varun Jampani, Yael Pritch, Michael Rubinstein, and Kfir Aberman.
 584 Dreambooth: Fine tuning text-to-image diffusion models for subject-driven generation. In *Proceed-
 585 ings of the IEEE/CVF conference on computer vision and pattern recognition*, pp. 22500–22510,
 586 2023.

587 Yuyang Shi, Valentin De Bortoli, Andrew Campbell, and Arnaud Doucet. Diffusion schrödinger
 588 bridge matching. *Advances in Neural Information Processing Systems*, 36:62183–62223, 2023.

594 Gyumin Shim, Jinsun Park, and In So Kweon. Robust reference-based super-resolution with similarity-
 595 aware deformable convolution. In *Proceedings of the IEEE/CVF conference on computer vision*
 596 and pattern recognition, pp. 8425–8434, 2020.

597

598 Haoze Sun, Wenbo Li, Jianzhuang Liu, Haoyu Chen, Renjing Pei, Xueyi Zou, Youliang Yan, and
 599 Yujiu Yang. Coser: Bridging image and language for cognitive super-resolution. In *Proceedings of*
 600 *the IEEE/CVF Conference on Computer Vision and Pattern Recognition*, pp. 25868–25878, 2024.

601

602 Zachary Teed and Jia Deng. Raft: Recurrent all-pairs field transforms for optical flow. In *Computer*
 603 *Vision–ECCV 2020: 16th European Conference, Glasgow, UK, August 23–28, 2020, Proceedings,*
 604 *Part II 16*, pp. 402–419. Springer, 2020.

605

606 Jianyi Wang, Kelvin CK Chan, and Chen Change Loy. Exploring clip for assessing the look and
 607 feel of images. In *Proceedings of the AAAI conference on artificial intelligence*, volume 37, pp.
 608 2555–2563, 2023a.

609

610 Jianyi Wang, Zongsheng Yue, Shangchen Zhou, Kelvin CK Chan, and Chen Change Loy. Exploiting
 611 diffusion prior for real-world image super-resolution. *International Journal of Computer Vision*,
 132(12):5929–5949, 2024.

612

613 Xintao Wang, Liangbin Xie, Chao Dong, and Ying Shan. Real-esrgan: Training real-world blind
 614 super-resolution with pure synthetic data. In *Proceedings of the IEEE/CVF international conference*
 615 *on computer vision*, pp. 1905–1914, 2021.

616

617 Zhengyi Wang, Cheng Lu, Yikai Wang, Fan Bao, Chongxuan Li, Hang Su, and Jun Zhu. Pro-
 618 lificdreamer: High-fidelity and diverse text-to-3d generation with variational score distillation.
Advances in Neural Information Processing Systems, 36:8406–8441, 2023b.

619

620 Zhou Wang, Alan C Bovik, Hamid R Sheikh, and Eero P Simoncelli. Image quality assessment: from
 621 error visibility to structural similarity. *IEEE transactions on image processing*, 13(4):600–612,
 2004.

622

623 Rongyuan Wu, Lingchen Sun, Zhiyuan Ma, and Lei Zhang. One-step effective diffusion network
 624 for real-world image super-resolution. *Advances in Neural Information Processing Systems*, 37:
 625 92529–92553, 2024a.

626

627 Rongyuan Wu, Tao Yang, Lingchen Sun, Zhengqiang Zhang, Shuai Li, and Lei Zhang. Seesr:
 628 Towards semantics-aware real-world image super-resolution. In *Proceedings of the IEEE/CVF*
 629 *conference on computer vision and pattern recognition*, pp. 25456–25467, 2024b.

630

631 Zhongcong Xu, Jianfeng Zhang, Jun Hao Liew, Hanshu Yan, Jia-Wei Liu, Chenxu Zhang, Jiashi
 632 Feng, and Mike Zheng Shou. Magicanimate: Temporally consistent human image animation using
 633 diffusion model. In *Proceedings of the IEEE/CVF Conference on Computer Vision and Pattern*
 634 *Recognition*, pp. 1481–1490, 2024.

635

636 Fuzhi Yang, Huan Yang, Jianlong Fu, Hongtao Lu, and Baining Guo. Learning texture transformer
 637 network for image super-resolution. In *Proceedings of the IEEE/CVF conference on computer*
 638 *vision and pattern recognition*, pp. 5791–5800, 2020.

639

640 Sidi Yang, Tianhe Wu, Shuwei Shi, Shanshan Lao, Yuan Gong, Mingdeng Cao, Jiahao Wang, and
 641 Yujiu Yang. Maniq: Multi-dimension attention network for no-reference image quality assessment.
 In *Proceedings of the IEEE/CVF conference on computer vision and pattern recognition*, pp. 1191–
 1200, 2022.

642

643 Fanghua Yu, Jinjin Gu, Zheyuan Li, Jinfan Hu, Xiangtao Kong, Xintao Wang, Jingwen He, Yu Qiao,
 644 and Chao Dong. Scaling up to excellence: Practicing model scaling for photo-realistic image
 645 restoration in the wild. In *Proceedings of the IEEE/CVF Conference on Computer Vision and*
646 Pattern Recognition, pp. 25669–25680, 2024.

647

Lin Zhang, Lei Zhang, and Alan C Bovik. A feature-enriched completely blind image quality
 evaluator. *IEEE Transactions on Image Processing*, 24(8):2579–2591, 2015.

648 Lin Zhang, Xin Li, Dongliang He, Fu Li, Errui Ding, and Zhaoxiang Zhang. Lmr: a large-scale
649 multi-reference dataset for reference-based super-resolution. In *Proceedings of the IEEE/CVF*
650 *International Conference on Computer Vision*, pp. 13118–13127, 2023a.
651
652 Lvmi Zhang, Anyi Rao, and Maneesh Agrawala. Adding conditional control to text-to-image
653 diffusion models. In *Proceedings of the IEEE/CVF international conference on computer vision*,
654 pp. 3836–3847, 2023b.
655
656 Richard Zhang, Phillip Isola, Alexei A Efros, Eli Shechtman, and Oliver Wang. The unreasonable
657 effectiveness of deep features as a perceptual metric. In *Proceedings of the IEEE conference on*
658 *computer vision and pattern recognition*, pp. 586–595, 2018.
659
660 Zhifei Zhang, Zhaowen Wang, Zhe Lin, and Hairong Qi. Image super-resolution by neural texture
661 transfer. In *Proceedings of the IEEE/CVF conference on computer vision and pattern recognition*,
662 pp. 7982–7991, 2019.
663
664 Haitian Zheng, Mengqi Ji, Haoqian Wang, Yebin Liu, and Lu Fang. Crossnet: An end-to-end
665 reference-based super resolution network using cross-scale warping. In *Proceedings of the Euro-*
666 *pean conference on computer vision (ECCV)*, pp. 88–104, 2018.
667
668 Han Zou, Masanori Suganuma, and Takayuki Okatani. Refvsr++: Exploiting reference inputs for
669 reference-based video super-resolution. In *2025 IEEE/CVF Winter Conference on Applications of*
670 *Computer Vision (WACV)*, pp. 2756–2765. IEEE, 2025.
671
672
673
674
675
676
677
678
679
680
681
682
683
684
685
686
687
688
689
690
691
692
693
694
695
696
697
698
699
700
701

702 A THE USE OF LARGE LANGUAGE MODELS (LLMs)

704 We used large language models (LLMs) only to polish the writing and check grammar. They were
 705 not used to generate ideas, design methods, or influence experimental results.
 706

707 B MORE IMPLEMENTATION DETAILS

709 B.1 LOSS DETAILS

711 We define the forward process of the flow matching as,
 712

$$713 z_t = \alpha(t)z_{Hs} + \beta(t)z_{Ls} + \sigma(t)\epsilon, \quad (8)$$

714 and the objective:

$$716 \mathcal{L}_\theta = \mathbb{E}_{t, z_t} \|G_\theta(z_t, t) - \frac{dz_t}{dt}\|_2^2. \quad (9)$$

717 Specifically, we define the coefficients as,
 718

$$719 \alpha(t) = \frac{(1-t)(0.2-t)}{0.2}, \quad \beta(t) = \frac{(1-t)t}{0.2}, \quad (10)$$

$$721 \sigma(t) = t, \quad \text{with } t \in [0, 0.2]. \quad (11)$$

722 It can be observed that $\alpha(t)$, $\beta(t)$ and $\sigma(t)$ are differentiable and sum to 1 for every t . Moreover,
 723 when $t = 0$, $z_t = z_{Hs}$, and when $t = 0.2$, $z_t = 0.8z_{Ls} + 0.2\epsilon$. This formulation adheres to the flow-
 724 matching framework, with the only deviation from the classical setup being the initial distribution:
 725 instead of pure Gaussian noise, we use a biased mixture defined as $z_{mix} = 0.8z_{Ls} + 0.2\epsilon$. The
 726 learning objective is to estimate a velocity field that transports $z_{mix} \rightarrow z_{Hs}$ within a narrow time
 727 window of length 0.2.

728 The core intuition is that low-quality (*i.e.*, z_{Ls}) and high-quality (*i.e.*, z_{Hs}) images share most of
 729 their low-frequency information. In other words, the primary difference between them lies in the
 730 high-frequency details. As a result, applying the full computational cost of denoising a completely
 731 random image—as is done in classical diffusion or flow-matching approaches—is largely inefficient.

732 Therefore, we apply only a 20% Gaussian noise perturbation, which preserves low-frequency information
 733 while introducing stochasticity to maintain a well-posed learning problem, *e.g.*, preventing
 734 the collapse of the generative diffusion prior. Furthermore, the ODE is integrated over a shortened
 735 time interval, $t \in [0, 0.2]$, significantly reducing the sampling path length. As a result, our inference
 736 process requires only 6 sampling steps, making it substantially faster than most diffusion-based image
 737 generation models. More importantly, due to the reduced stochasticity, the predictions become more
 738 deterministic—an advantageous property in image restoration scenarios where consistency is critical.
 739

740 B.2 TRAINING DETAILS

741 Following prior work, we perform cross-attention across all DiTs in Stable Diffusion 3-medium for
 742 full feature fusion, involving both image and text embeddings. Since the reference image provides
 743 rich structural and textural cues, we use an empty text prompt during training and inference. We
 744 fine-tune the image branches in both the DiT-based ReferenceNet and RestorationNet, while keeping
 745 the text branch fixed to fully exploit the HQ guidance.
 746

747 B.3 COMPARISONS ON COMPUTATIONAL COSTS

749 LiveMoments processes a **1024×1024 patch in 1.89 seconds** under FP16 inference on an H20 GPU
 750 (14.6 GB memory, 98.91 TFLOPs). For a 4K Live Photo (*i.e.*, 3072×4096), the total processing
 751 time is about **40 seconds**. To further clarify the computational cost, we report the parameter count,
 752 as well as the parameter-only VRAM and the inference-time peak VRAM for all components of
 753 LiveMoments in Tab. 4, measured when processing a 4K Live Photo.

754 We also provide a detailed comparison of parameter count, FLOPs, peak memory usage, and inference
 755 time between our method and the diffusion-based RefISR and SISR methods. All measurements
 756 were conducted on a single NVIDIA H20 GPU and run in mixed precision under a resolution of

756
757
758
759
760
761
762
763
764
765
766
767
768
769
770
771
772
773
774
775
776
777
778
779
780
781
782
783
784
785
786
787
788
789
790
791
792
793
794
795
796
797
798
799
800
801
802
803
804
805
806
807
808
809
Table 4: Comparisons on branch-wise parameter counts and VRAM, measured when processing a 4K Live Photo.

Component	Parameter Counts (M)	Parameter-only VRAM (MB)	Inference-time Peak VRAM (MB)
VAE	83.82	159.87	12368.33
ReferenceNet	2028.33	3868.73	10090.78
RestorationNet	2084.95	3976.73	10091.28
RAFT	5.26	10.03	13180.38
Motion Encoder	66.09	126.06	9940.00

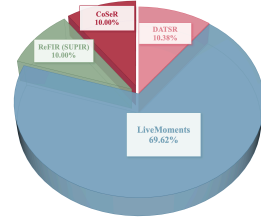
764
765
766
767
768
769
770
771
772
773
774
775
776
777
778
779
780
781
782
783
784
785
786
787
788
789
790
791
792
793
794
795
796
797
798
799
800
764
765
766
767
768
769
770
771
772
773
774
775
776
777
778
779
780
781
782
783
784
785
786
787
788
789
790
791
792
793
794
795
796
797
798
799
800
Table 5: Comparisons with RefISR and SISR methods on parameter counts, FLOPs, peak memory usage and inference time at a resolution of 1024×1024 on a single NVIDIA H20 GPU.

Type	Method	Parameter Counts (M)	TFLOPs	Peak Memory (GB)	Inference Time (s)
Time-Step Distilled Methods	OSEDiff	1294.38 + 470.93 (DAPE)	20.53	8.66	0.43
	TSD-SR	2207.33	21.91	8.60	0.24
	CoSeR	2655.52	—	32.74	48.83
	ReFIR (SeeSR)	2039.83 + 470.93 (DAPE)	1560.70	17.83	27.62
	ReFIR (SUPIR)	4801.18	2672.70	59.82	31.67
	StableSR	1554.64	2236.31	34.53	164.67
	DiffBIR	1683.45	691.43	35.46	26.02
	SeeSR	2039.83 + 470.93 (DAPE)	741.42	12.07	14.54
	SUPIR	4801.18	1200.65	54.25	16.98
	LiveMoments	4268.45	98.91	14.53	1.89

1024 \times 1024, except for CoSeR and DiffBIR, which do not support mixed precision inference at that resolution. As shown in Tab. 5, our LiveMoments achieves the lowest TFLOPs and the shortest inference time among the multi-step methods, while maintaining a competitive model size and peak memory usage to others. Although one-step diffusion methods such as OSEDiff and TSDSR benefit from distillation-based training and therefore exhibit faster inference and lower computational cost, LiveMoments achieves a trade-off between computational cost and restoration quality.

C USER STUDY

787
788
789
790
791
792
793
794
795
796
797
798
799
800
We compare LiveMoments with three representative RefSR methods: a traditional method (DATSR), a diffusion-based approach (ReFIR), and the strongest quantitative baseline (CoSeR). A total of 26 participants took part in the vote. They were asked to select the result that best matches the visual quality of the reference while preserving the content of the reselected LQ frame. As shown in Fig. 6, our method receives 69.62% approval rates, indicating its effectiveness.

797
798
799
800
Figure 6: User study results.

D MORE ANALYSIS OF THE PROPOSED RELATIVE NO-REFERENCE METRICS

D.1 CORRELATION BETWEEN RELATIVE NO-REFERENCE METRICS AND HUMAN PREFERENCES

801
802
803
804
805
806
807
808
809
Using the same three baselines as in the main user study (DATSR, ReFIR, and CoSeR), we further conducted a ranking-based experiment to analyze the correlation between the relative no-reference metrics and human preferences. We randomly sampled 15 images from vivoLive144 and 10 images from iPhoneLive90. A total of 15 participants are invited to rank the images based on perceptual similarity to the reference.

In Tab. 6, the Spearman and Pearson correlations show that all four metrics maintain positive, moderate alignment with human perception across devices and ISPs. These values are comparable to those reported in generic NR-IQA methods without task-specific training such as CLIPQA (typically 0.36–0.74), despite our much smaller real-world dataset. This indicates that the proposed relative no-reference metrics remain meaningfully correlated with human perception.

810
811
812
813
814
815
816
817
Table 6: Spearman and Pearson correlations between relative no-reference metrics and human
perception on real-world Live Photo datasets.

Metric	vivoLive144		iPhoneLive90	
	Spearman↑	Pearson↑	Spearman↑	Pearson↑
NIQE _{re}	0.493	0.518	0.604	0.560
MUSIQ _{re}	0.585	0.543	0.414	0.440
CLIPQA _{re}	0.558	0.542	0.486	0.495
MANIQA _{re}	0.535	0.548	0.370	0.413

✗ preferred by no-reference metrics	✓ preferred by human & relative-reference metrics	✗ preferred by no-reference metrics	✓ preferred by human & relative-reference metrics
CoSeR	LiveMoments	aligned key photo	TSDSR
			
CLIPQA↑: 0.5867 CLIPQA _{re} ↓: 0.2224 MANIQA↑: 0.5033 MANIQA _{re} ↓: 0.1184	CLIPQA↑: 0.4266 CLIPQA _{re} ↓: 0.1112 MANIQA↑: 0.4235 MANIQA _{re} ↓: 0.0588		NIQE↓: 2.0735 NIQE _{re} ↓: 0.4873 CLIPQA↑: 0.7990 CLIPQA _{re} ↓: 0.1901
SeeSR	LiveMoments	aligned key photo	ReFIR (SeeSR)
			
MUSIQ↑: 54.68 MUSIQ _{re} ↓: 0.0308 CLIPQA↑: 0.6246 CLIPQA _{re} ↓: 0.5199	MUSIQ↑: 52.37 MUSIQ _{re} ↓: 0.0126 CLIPQA↑: 0.4153 CLIPQA _{re} ↓: 0.0104		MUSIQ↑: 54.67 MUSIQ _{re} ↓: 0.3663 CLIPQA↑: 0.5203 CLIPQA _{re} ↓: 0.3054
SUPIR	LiveMoments	aligned key photo	ReFIR (SUPIR)
			
NIQE↓: 3.7756 NIQE _{re} ↓: 0.3111 MUSIQ↑: 55.61 MUSIQ _{re} ↓: 0.1828	NIQE↓: 4.2253 NIQE _{re} ↓: 0.2291 MUSIQ↑: 50.70 MUSIQ _{re} ↓: 0.0783		CLIPQA↑: 0.3558 CLIPQA _{re} ↓: 0.6378 MANIQA↑: 0.4587 MANIQA _{re} ↓: 0.1764

818
819
820
821
822
823
824
825
826
827
828
829
830
831
832
833
834
835
836
837
838
839
840
841
842
843
844
845
846
847
Figure 7: Comparison between no-reference metrics, the proposed relative no-reference metrics, and human visual preference in evaluating the key photo reselection task. The aligned key photo is cropped manually for better comparison.851
852
853
854
855
856
857
858
859
860
861
862
863
D.2 COMPARISON OF NO-REFERENCE METRICS WITH THE PROPOSED RELATIVE
NO-REFERENCE METRICS864
865
866
867
868
869
870
871
872
873
874
875
876
877
878
879
880
881
882
883
884
885
886
887
888
889
890
891
892
893
894
895
896
897
898
899
900
We present additional experiments in Fig. 7 to demonstrate that the widely-used no-reference metrics
may have limitations in assessing image quality under the task of key photo reselection. It can be
observed that these metrics prefer rich texture but far from real appearance results.

E ADDITIONAL ABLATION RESULTS

E.1 ABLATION STUDY ON SYN LIVE260 DATASET

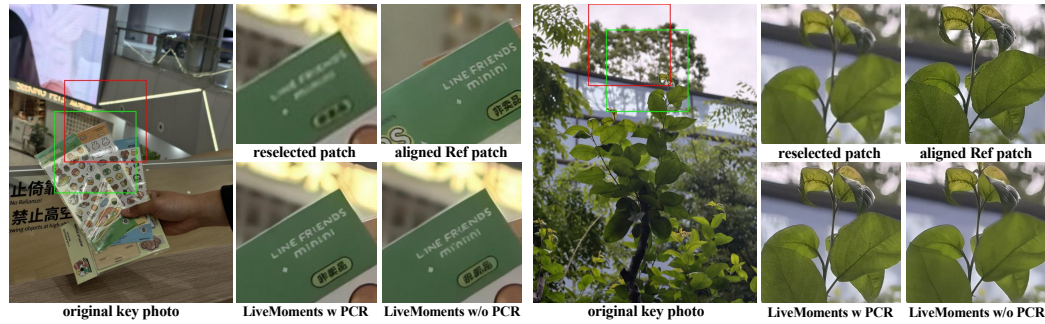
901
902
903
904
905
906
907
908
909
910
911
912
913
914
915
916
917
918
919
920
921
922
923
924
925
926
927
928
929
930
931
932
933
934
935
936
937
938
939
940
941
942
943
944
945
946
947
948
949
950
951
952
953
954
955
956
957
958
959
960
961
962
963
964
965
966
967
968
969
970
971
972
973
974
975
976
977
978
979
980
981
982
983
984
985
986
987
988
989
990
991
992
993
994
995
996
997
998
999
We additionally provide ablation results on SynLive260 with ground-truth in Table 7. While our
method does not achieve the absolute best scores in distortion-oriented metrics such as PSNR and

864 Table 7: Ablation study of the network design on SynLive260. All warp operation is applied on the
 865 original key photo, denoted as the reference image (Ref). The best results are highlighted in **bold**.
 866 Here, CA_{re} denotes CLIPQA and MA_{re} denotes MANIQA.
 867

Method	PSNR↑	SSIM↑	LPIPS↓	DISTS↓	$CA_{re} \downarrow$	$MA_{re} \downarrow$	CLIP-Q↑	DINO-Q↑
RestorationNet	30.42	0.8610	0.1685	0.0793	0.1721	0.0927	0.9841	0.9195
RestorationNet + ReferenceNet	31.47	0.8980	0.0837	0.0388	0.1246	0.0586	0.9949	0.9643
RestorationNet + ReferenceNet + warp RefImage	31.49	0.8927	0.0968	0.0475	0.1569	0.0546	0.9934	0.9556
RestorationNet + ReferenceNet + warp RefLatent	31.84	0.8986	0.0924	0.0441	0.1305	0.0618	0.9936	0.9566
RestorationNet + ReferenceNet + warp RefKV	31.82	0.8991	0.0895	0.0435	0.1306	0.0645	0.9940	0.9580
LiveMoments (full model)	31.65	0.8990	0.0828	0.0365	0.1155	0.0495	0.9950	0.9740

873 Table 8: Ablation study of different training degradation settings on vivoLive144. “Customized Live
 874 Photo degradation” is the setting used in the main experiments. Best results are highlighted in **bold**.
 875

Degradation Type	NIQE _{re} ↓	MUSIQ _{re} ↓	CLIPQA _{re} ↓	MANIQA _{re} ↓	CLIP-Q↑	DINO-Q↑
Moderate-StableSR	0.0925	0.1086	0.0883	0.0673	0.9786	0.9550
StableSR	0.0933	0.1165	0.1056	0.0734	0.9791	0.9581
SeeSR	0.0904	0.1030	0.0812	0.0647	0.9788	0.9505
Customized Live Photo Degradation	0.0990	0.0893	0.0809	0.0556	0.9805	0.9629



880 Figure 8: Comparison between LiveMoments with (w) and without (w/o) the proposed Patch
 881 Correspondence Retrieval (PCR) strategy when processing 4K images. Patches are cropped for
 882 clearer visualization. Please zoom in for better view.
 883

884 SSIM, it consistently surpasses all baselines across perceptual and reference-based quality metrics
 885 (LPIPS, DISTS, CLIP-Q, DINO-Q, etc.). These results indicate that LiveMoments is more effective
 886 at recovering fine-grained structures and perceptual fidelity, aligning better with human perception.
 887 The consistent performance on both synthetic and real data further confirms the robustness and
 888 effectiveness of our design.
 889

900 E.2 MORE VISUAL EXAMPLES FOR PATCH CORRESPONDENCE RETRIEVAL (PCR)

902 To further validate the effectiveness of our Patch Correspondence Retrieval (PCR) strategy, we
 903 provide additional challenging cases in Fig. 8. Even under large motion and complex textures, PCR
 904 corrects spatial offsets between degraded and reference patches, enabling accurate transfer of fine
 905 details such as text edges and leaf veins. These results confirm that PCR enhances both restoration
 906 fidelity and fine-grained detail recovery in high-resolution scenarios.
 907

908 E.3 ANALYSIS ON DEGRADATION SETTINGS

909 We conducted analyses to explore how different synthetic degradation settings affect real-world
 910 performance. Specifically, we trained LiveMoments under three representative degradation settings:
 911 (1) SeeSR degradation, (2) StableSR degradation, and (3) a lighter moderate-StableSR variant
 912 constructed by reducing the blur and noise levels. The quantitative results on vivoLive144 are
 913 reported in Tab. 8. Among the three settings, our customized Live Photo degradation achieves the
 914 best results across most metrics, indicating that it better reflects real-world degradation characteristics.
 915 At the same time, LiveMoments maintains stable performance under all three degradation variants,
 916 demonstrating its robustness to different synthetic degradation.
 917

We also provide the visualizations of degraded images in Fig. 9. For each setting, the synthetic
 degradation is applied to the original key photo from our real-world Live Photo dataset and compared

Table 9: Ablation study of robustness analysis under flow noise injection and flow estimator replacement on vivoLive144. Best results are highlighted in **bold**.

Method	NIQE _{re} ↓	MUSIQ _{re} ↓	CLIPQA _{re} ↓	MANIQA _{re} ↓	CLIP-Q↑	DINO-Q↑
LiveMoments + 10% noise	0.0999	0.0921	0.0808	0.0561	0.9802	0.9622
LiveMoments + 20% noise	0.1035	0.0935	0.0802	0.0551	0.9799	0.9613
LiveMoments + 40% noise	0.1082	0.0993	0.0811	0.0546	0.9792	0.9591
LiveMoments + 80% noise	0.1108	0.1072	0.0845	0.0548	0.9785	0.9555
LiveMoments + 100% noise	0.1116	0.1099	0.0862	0.0566	0.9782	0.9540
LiveMoments + 200% noise	0.1159	0.1222	0.0915	0.0578	0.9771	0.9497
LiveMoments (SPyNet)	0.1006	0.0907	0.0809	0.0561	0.9804	0.9629
LiveMoments (LiteFlowNet)	0.1031	0.0946	0.0808	0.0544	0.9794	0.9595
LiveMoments	0.0990	0.0893	0.0809	0.0556	0.9805	0.9629

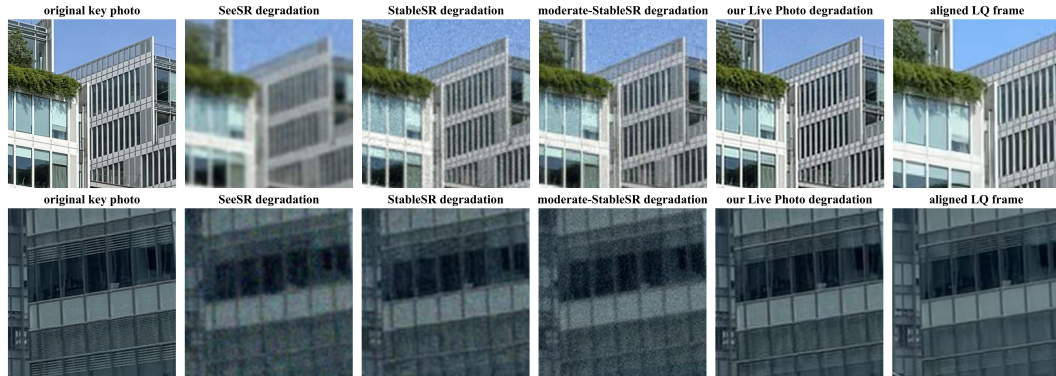


Figure 9: Comparison between different degradation settings. The aligned LQ is cropped manually for better comparison. Please zoom in for better view.

with the corresponding reselected LQ frame, allowing us to assess how well the synthetic degradations replicate real degradation patterns. The results show that existing settings tend to apply stronger degradations than those observed in real Live Photos, while our customized Live Photo degradations more faithfully reflect real-world characteristics.

E.4 ROBUSTNESS ANALYSIS OF INACCURATE MOTION ALIGNMENT

We analyze the behavior and robustness of LiveMoments when the estimated optical flow is inaccurate and motion alignment becomes unreliable. To quantify its sensitivity to flow errors, we conduct two analyses on vivoLive144: (1) perturbing the RAFT flow with Gaussian noise, and (2) replacing RAFT with alternative flow estimators. The results are provided in Tab. 9.

Noise Injection. We add Gaussian noise with different magnitudes (10%–200% of the original flow magnitude) to the RAFT outputs. Although the perturbed flows become increasingly distorted, the reconstruction quality of LiveMoments degrades only slightly under moderate perturbations, indicating low sensitivity to flow inaccuracies.

Flow Estimator Replacement. We substitute RAFT with SPyNet and LiteFlowNet, and the results remain close to the original RAFT-based LiveMoments, suggesting that the model does not rely on a specific flow estimator and generalizes across different motion estimation methods.

In addition, we provide visualizations to further analyze the impact of flow errors, including the reselected LQ frame, the original key photo with optical flow, and the warped original key photo, together with cropped regions that illustrate local refinement quality.

Robust cases. As shown in Fig. 10, LiveMoments remains stable even when RAFT produces low-confidence or divergent flow vectors due to large motion or occlusion. Despite inaccurate motion guidance, the model does not introduce hallucinated textures and still produces visually coherent results, demonstrating its robustness to moderate flow errors.

Failure cases. In Fig. 11, we provide failure-case visualizations, including examples with large motion, severe occlusion, and low-texture regions that lead to inaccurate flow. These examples reveal the boundary conditions where motion alignment errors exceed the model’s ability to compensate.

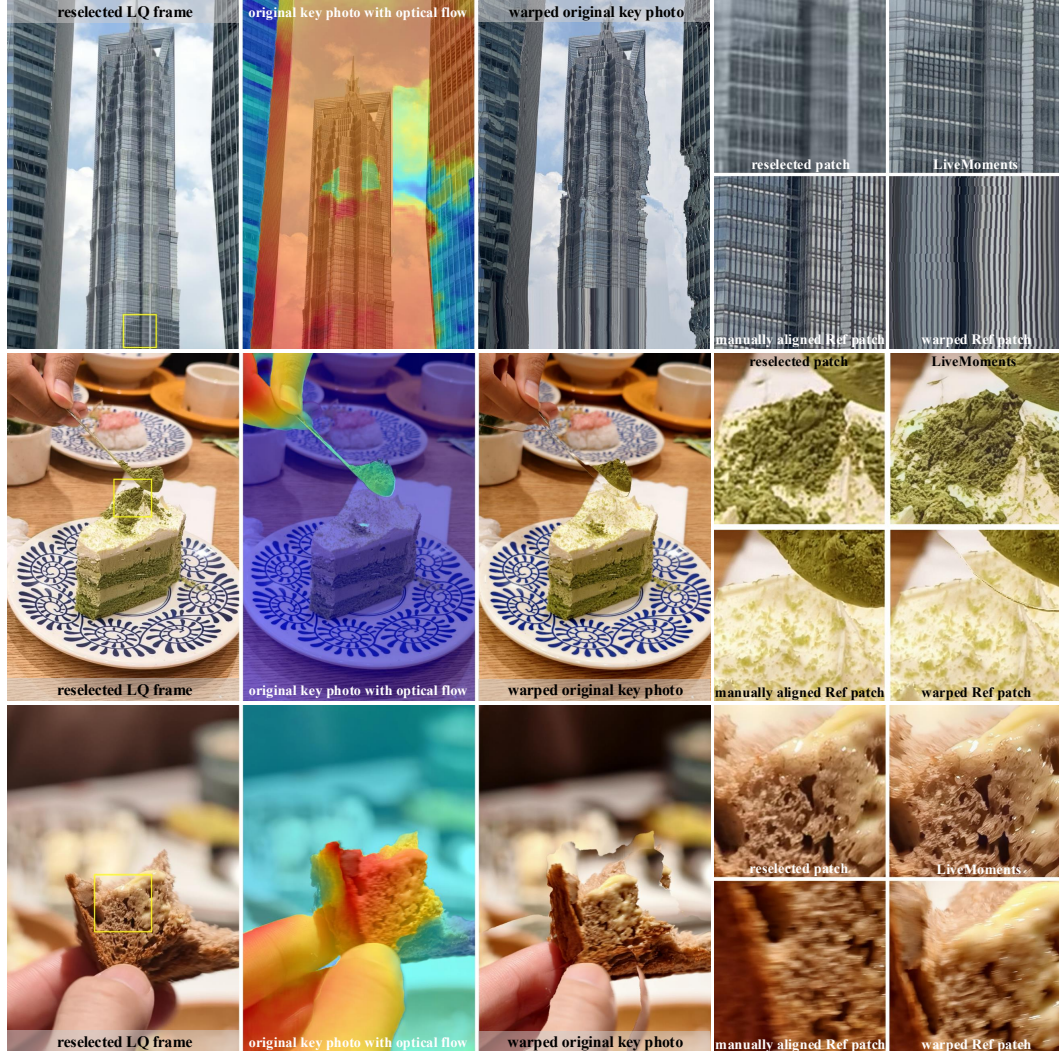


Figure 10: Robust cases with inaccurate motion alignment. The aligned original key photo is cropped manually for better comparison. Please zoom in for better view.

F MORE VISUAL RESULTS

In Figs. 12, 13, 14 and 16, we present additional visual comparisons on the real world Live Photo dataset **vivoLive144**, including cases under high-resolution scenes. We compare visual results on vivoLive144 from other RefISR, RefVSR and SISR baselines in Fig. 15. In Figs. 17 and 18, we present additional visual comparisons and high-resolution results on **iPhoneLive90**. The visual results of iPhoneLive90 from other RefISR, RefVSR and SISR baselines are provided in Fig. 19. In Figs. 19 and 20, we present additional visual comparisons and high-resolution results on **SynLive260**. These examples demonstrate the robustness of LiveMoments in addressing the key photo re-selection task across scenarios.

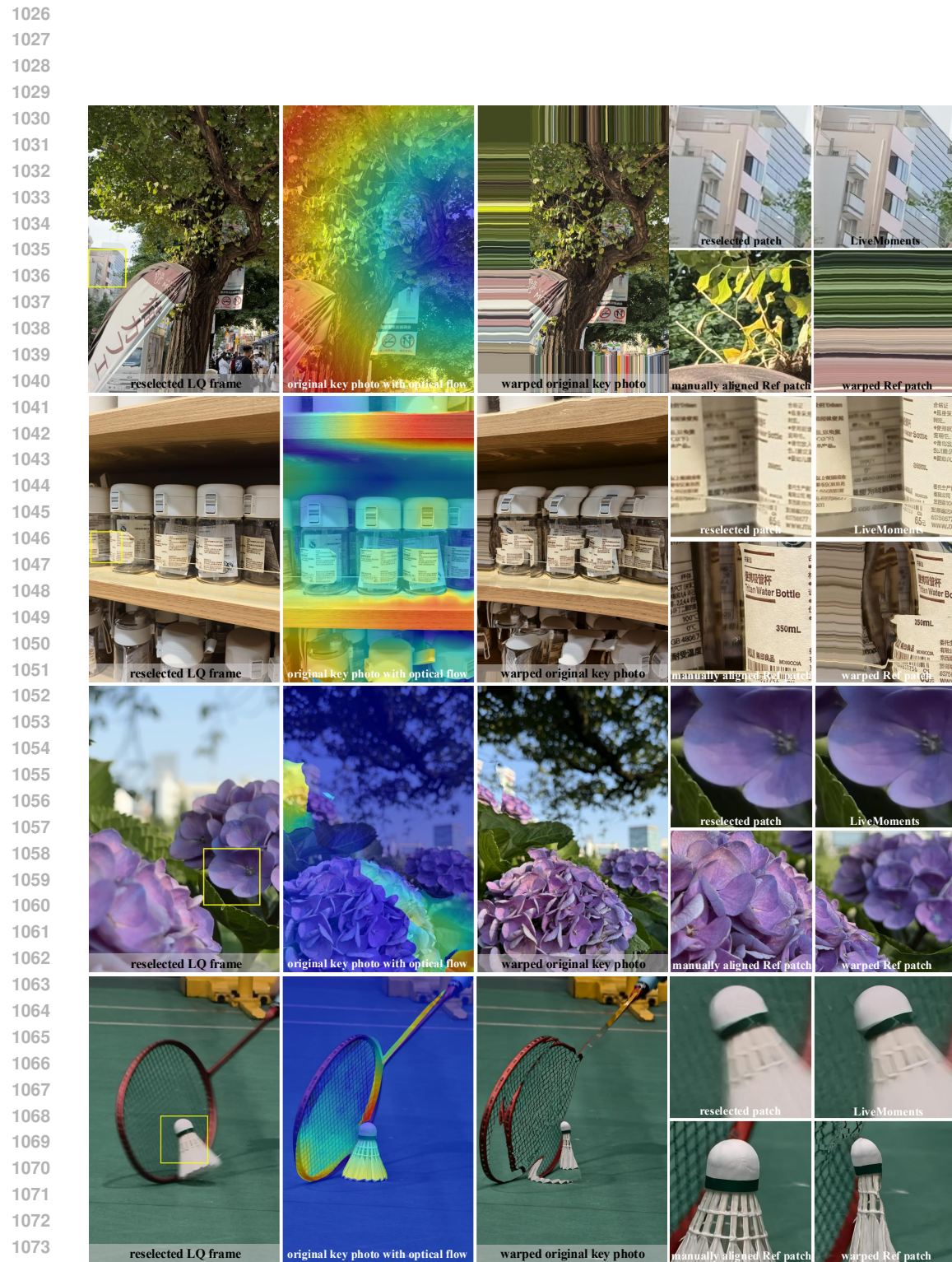


Figure 11: Failure cases with inaccurate motion alignment. The aligned original key photo is cropped manually for better comparison. Please zoom in for better view.

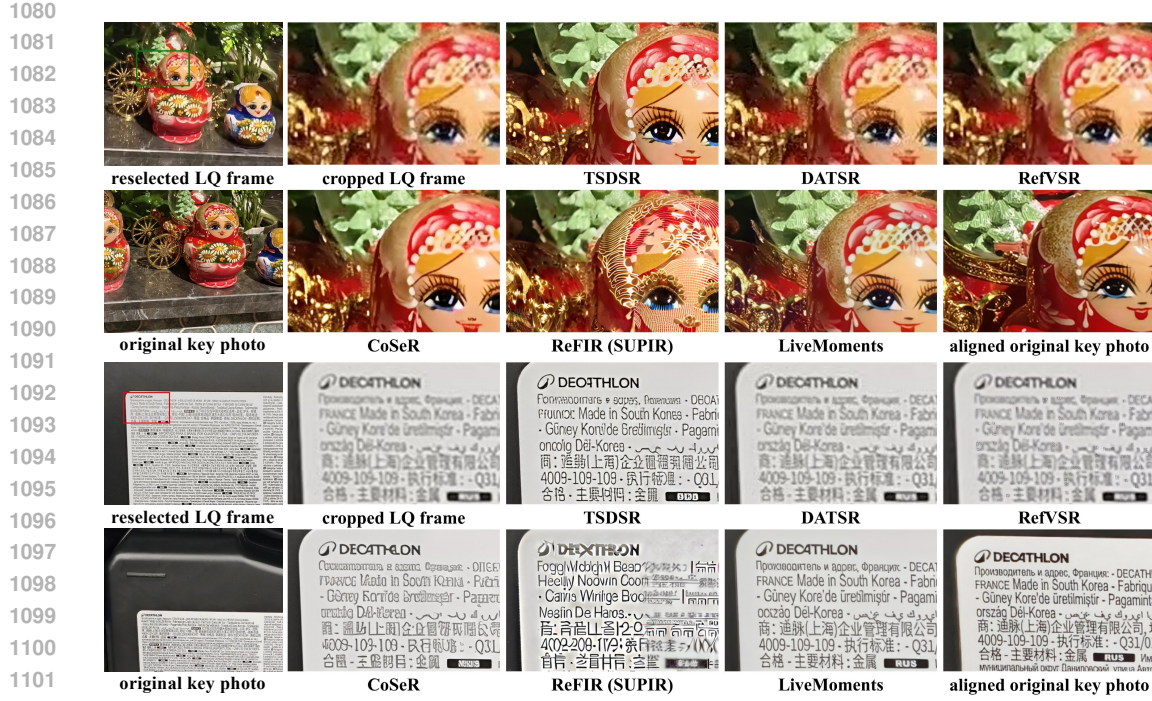


Figure 12: More visual comparisons of RefISR, RefVSR and SISR methods on vivoLive140 dataset. The aligned original key photo is cropped manually for comparison. Please zoom in for a better view.



Figure 13: High-resolution visual comparisons of diffusion-based RefISR methods on vivoLive140 dataset. The aligned original key photo is cropped manually for better comparison.



1161
1162
Figure 14: High-resolution visual comparisons of diffusion-based RefISR methods on vivoLive140
1163
1164
1165
1166
1167
1168
1169
1170
1171
1172
1173
1174
1175
1176
1177
1178
1179
1180
1181
1182
1183
1184
1185
1186
1187

dataset. The aligned original key photo is cropped manually for better comparison.

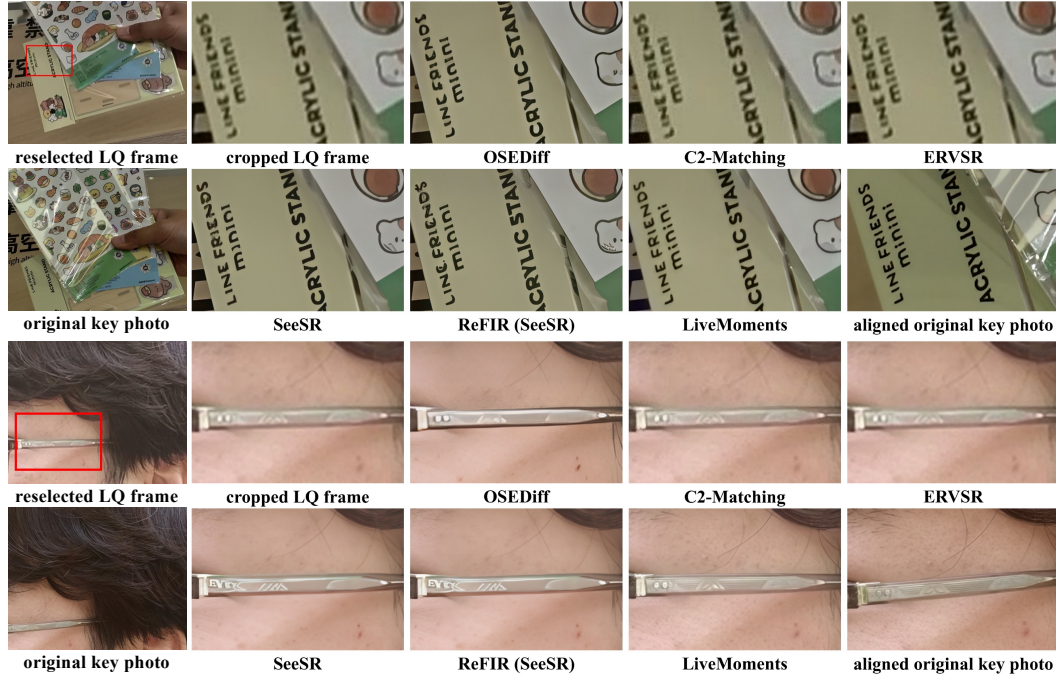


Figure 15: More visual comparisons of other RefISR, RefVSR and SISR methods on vivoLive140 dataset. The aligned original key photo is cropped manually for better comparison. Please zoom in for a better view.



1215
 1216
 1217
 1218
 1219
 1220
 1221
 1222
 1223
 1224
 1225
 1226
 1227
 1228
 1229
 1230
 1231
 1232
 1233
 1234
 1235
 1236
 1237
 1238
 1239
 1240
 1241

Figure 16: High-resolution visual comparisons of diffusion-based ReflISR methods on vivoLive140 dataset. The aligned original key photo is cropped manually for better comparison.

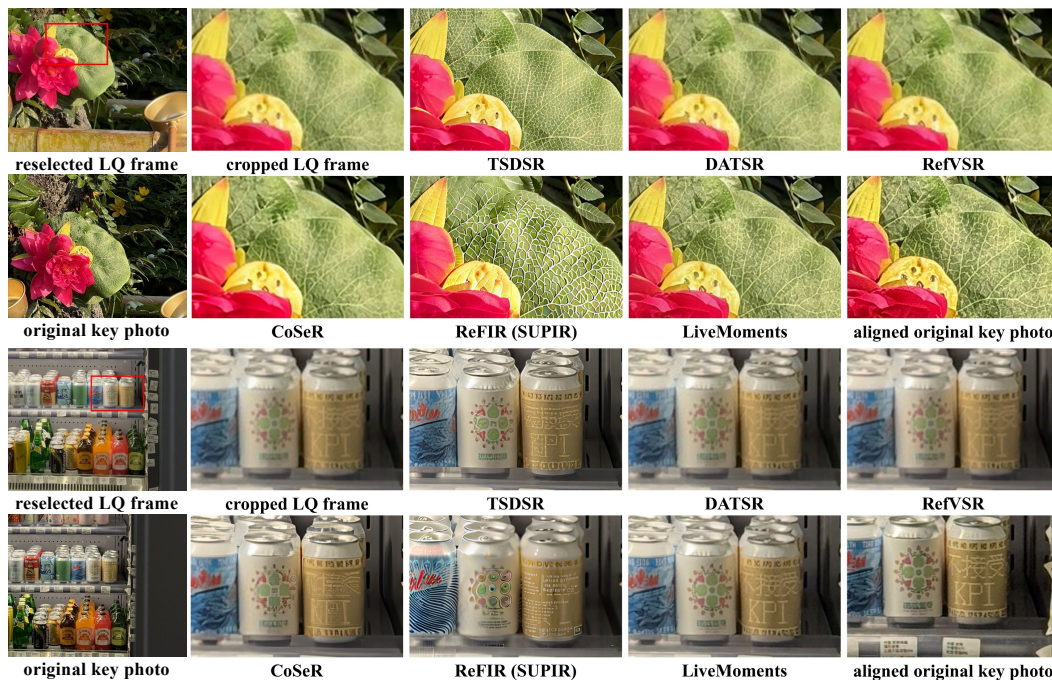


Figure 17: More visual comparisons of ReflISR, RefVSR and SISR methods on iPhoneLive90 dataset. The aligned original key photo is cropped manually for comparison. Please zoom in for a better view.

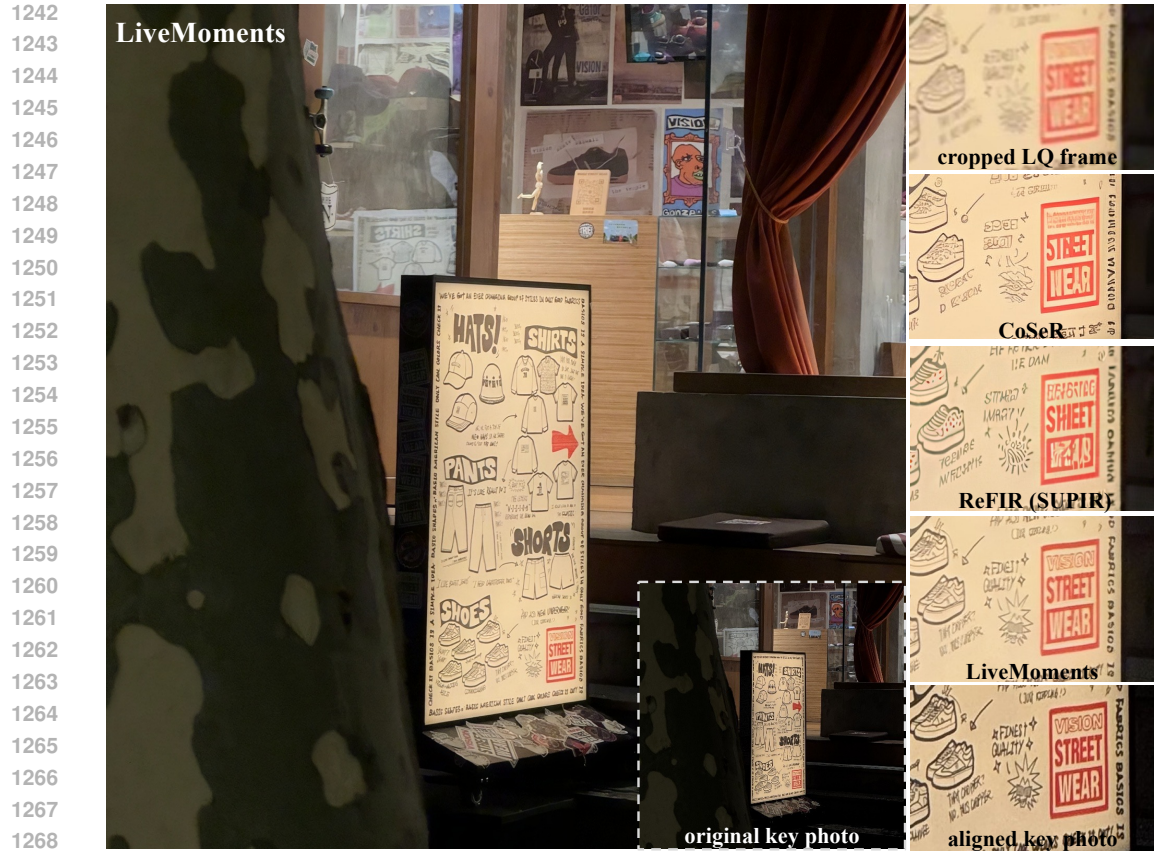


Figure 18: High-resolution visual comparisons of diffusion-based RefISR methods on iPhoneLive90 dataset. The aligned original key photo is cropped manually for better comparison.

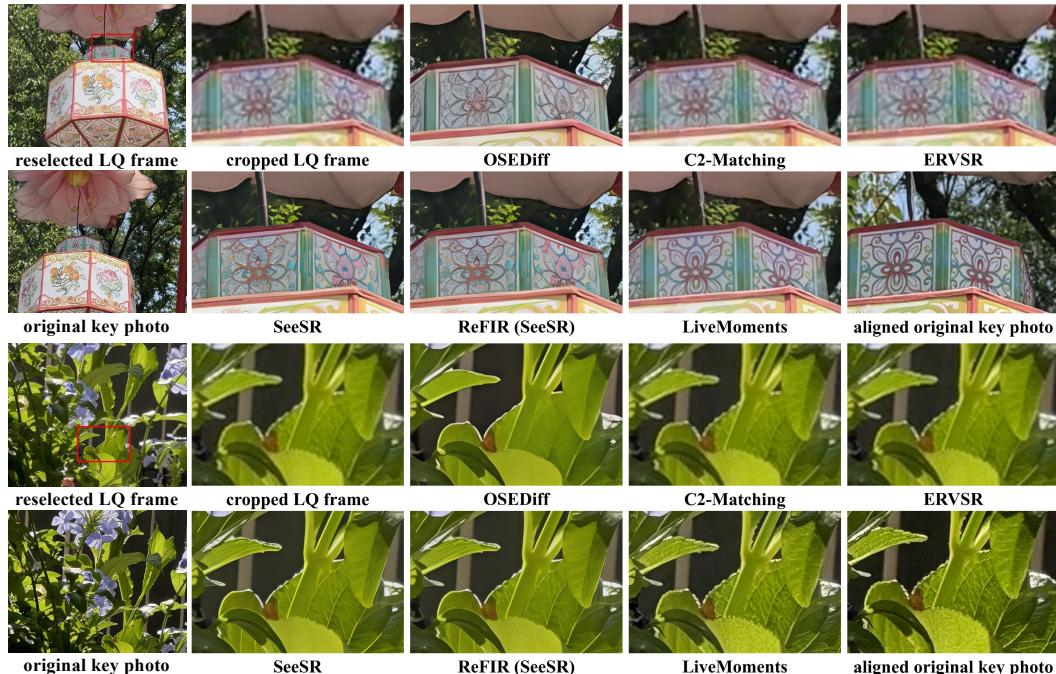


Figure 19: More visual comparisons of other RefISR, RefVSR and SISR methods on iPhoneLive90 dataset. The aligned original key photo is cropped manually for better comparison. Please zoom in for a better view.



1323
1324
1325
1326
1327
1328
1329
1330
1331
1332
1333
1334
1335
1336
1337
1338
1339
1340
1341
1342
1343
1344
1345
1346
1347
1348
1349

Figure 20: High-resolution visual comparisons of diffusion-based RefISR methods on SynLive260 dataset. The aligned original key photo is cropped manually for better comparison.

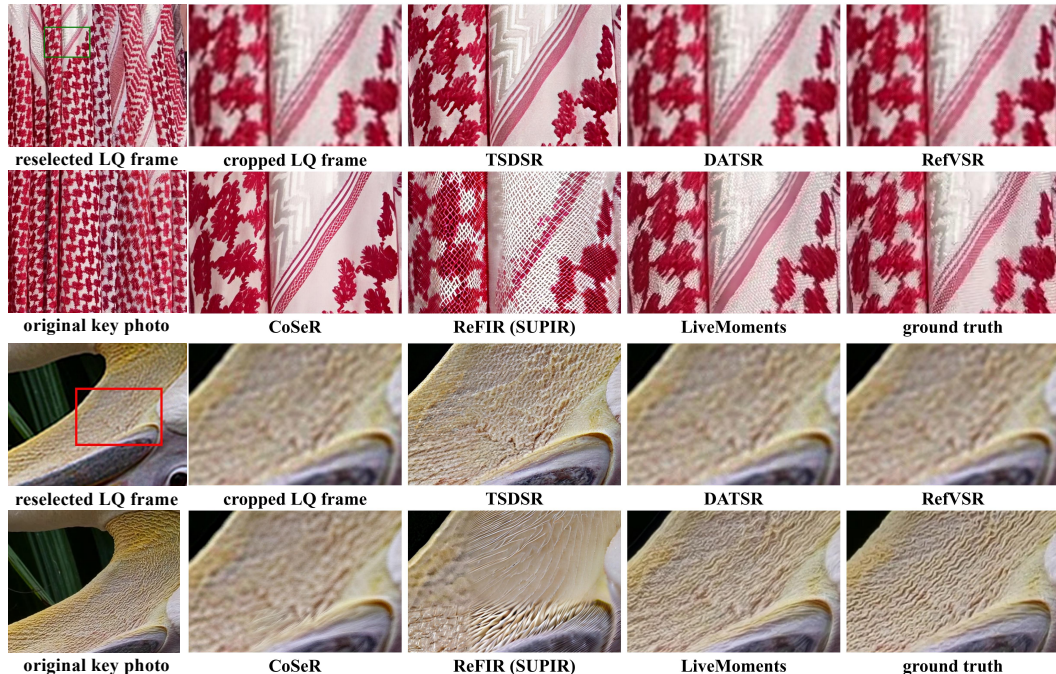


Figure 21: More visual comparisons of RefISR, RefVSR and SISR methods on SynLive260 dataset. The aligned original key photo is cropped manually for better comparison. Please zoom in for a better view.